Article

Deciphering the longitudinal trajectories of glioblastoma ecosystems by integrative single-cell genomics

A list of authors and their affiliations appears at the end of the paper

The evolution of isocitrate dehydrogenase (IDH)-wildtype glioblastoma (GBM) after standard-of-care therapy remains poorly understood. Here we analyzed matched primary and recurrent GBMs from 59 patients using single-nucleus RNA sequencing and bulk DNA sequencing, assessing the longitudinal evolution of the GBM ecosystem across layers of cellular and molecular heterogeneity. The most consistent change was a lower malignant cell fraction at recurrence and a reciprocal increase in glial and neuronal cell types in the tumor microenvironment (TME). The predominant malignant cell state differed between most matched pairs, but no states were exclusive or highly enriched in either time point, nor was there a consistent longitudinal trajectory across the cohort. Nevertheless, specific trajectories were enriched in subsets of patients. Changes in malignant state abundances mirrored changes in TME composition and baseline profiles, reflecting the co-evolution of the GBM ecosystem. Our study provides a blueprint of GBM's diverse longitudinal trajectories and highlights the treatment and TME modifiers that shape them.

Despite significant advances in basic and translational research, isocitrate dehydrogenase (IDH)-wildtype glioblastoma (GBM)[1] remains incurable. The standard treatment for newly diagnosed GBM consists of maximal surgical resection followed by radiotherapy and concurrent treatment with the alkylating agent temozolomide (TMZ). This treatment often elicits a partial response, particularly when the promoter of the O^6-methylguanine-DNA methyltransferase (MGMT) gene is methylated, as this gene encodes a DNA-repair protein that can remove alkyl groups added to O^6-methylguanine by TMZ. However, the disease invariably recurs with a median overall survival of 14.6 months[2,3]. To interrogate mechanisms of recurrence, several studies have analyzed the longitudinal evolution of GBM specimens[4–6]. The Glioma Longitudinal Analysis (GLASS) consortium reported high similarity in genetic driver alterations between primary and recurrent GBM, indicating that standard treatment does not exert substantial clonal selection[7]. Conversely, transcriptome and proteome studies have demonstrated more dynamic evolutionary patterns, such as a proneural-to-mesenchymal (MES) shift, enhanced neuronal signaling and upregulation of extracellular

matrix (ECM)-related genes at recurrence[5,6,8–14]. However, published longitudinal GBM studies have typically relied on bulk tissue profiling (averaging the signal across the malignant and tumor microenvironment (TME) compartments) and lack the granularity to independently interrogate the evolution of malignant and TME cell types and cell states. Single-cell longitudinal studies have had limited cohort size and limited clinical metadata, precluding a direct analysis of single-cell profiles with clinical correlates[14]. These limitations, along with the challenge of reconciling results from different groups that leverage diverse analytical and classification schemes, underscore the need for a larger single-cell longitudinal GBM dataset with detailed clinical and genomic annotations and with robust analysis.

We sought to address these challenges in two studies that we present here. We established the GBM Cellular Analysis of Resistance and Evolution (CARE) consortium to characterize the longitudinal evolutionary trajectories in GBM at single-cell resolution. We performed single-nuclei RNA sequencing (snRNA-seq) of paired primary and recurrent GBM samples from 59 patients with detailed clinical annotations

✉e-mail: axl4252@med.miami.edu; axi435@med.miami.edu; roel.verhaak@yale.edu; Itay.tirosh@weizmann.ac.il; suva.mario@mgh.harvard.edu

and genetic profiles. In the companion study of ref. 15, we conducted an analysis of the data independent of sampling time (primary versus recurrent) that characterized GBM transcriptional ecosystems across multiple layers. In this work, we examine the longitudinal changes in these ecosystems between primary and recurrence and identify molecular and clinical features that modify their trajectories. We show that a lower malignant cell fraction and a reciprocal increase in proportions of glial and neuronal (that is, glio-neural) TME cell types is the most consistent longitudinal change at recurrence, observed in 66% of cases. Contrary to prior studies, we observed no consistent malignant GBM state enrichment at recurrence across the cohort. However, specific trajectories were associated with defined subsets of cases, such as GBMs with *MGMT* methylation or radiation-related small deletion phenotype. Notably, changes in malignant state abundance were mirrored by corresponding changes in baseline profiles and TME composition, reflecting interdependent alterations of the GBM ecosystem. Our study highlights the diverse longitudinal GBM trajectories that are shaped by treatment response and TME interactions.

Results

Longitudinal profiling of a clinically annotated GBM cohort

We collected matched snap-frozen GBM specimens from primary and recurrent surgeries (Fig. 1a and Supplementary Table 1). Tumor samples were obtained from seven hospitals, resulting in a total of 121 tumors from 59 patients profiled by snRNA-seq and whole-exome sequencing (WES) or whole-genome sequencing (WGS; Fig. 1b; Methods). For the majority of patients, we profiled samples from two time points (labeled T1 and T2); for three patients, we profiled samples from three time points (T1, T2 and T3). Most matched sample pairs were derived from primary and first recurrent tumors, except for three pairs that consisted of two recurrent samples and four pairs that consisted of a primary and a second recurrence.

Tumor location was known for 51 patients, of whom 45 cases locally recurred at the surgical margin and six cases recurred at a site distant from the resection cavity. The majority of patients (51/59) received radiotherapy with concurrent TMZ and adjuvant TMZ following surgery. The improved clinical outcomes in our cohort (median interval between two surgeries = 12.4 months, median overall survival = 24 months), compared with historical cohorts, likely reflect better performance status of patients eligible for multiple surgical resections, consistent with a younger age at diagnosis (median = 53 years, range = 19–73 years).

In our 10x Genomics snRNA-seq dataset, 429,305 cells passed quality filters (Methods). Cells were classified as malignant (246,408 cells) or nonmalignant (182,897 cells) based on inferred chromosomal copy-number aberrations (CNA). Nonmalignant cells were further classified and annotated based on established cell-type signatures and marker gene expression[16–19] (Fig. 1c; Methods). Nonmalignant cells clustered together across time points (Fig. 1c, bottom), and we did not observe a significant difference in the number of cells profiled or the number of genes detected per cell between time points (Extended Data Fig. 1a,b).

Mutational and CNA profiles were derived from bulk DNA-sequencing data (Fig. 1b). The frequency of GBM driver alterations was consistent with prior studies[7] and remained largely stable across time points (Fig. 1d and Extended Data Fig. 1c). However, 26% of cases (14 of 54 patients) acquired treatment-related DNA hypermutation[20] or an increase in small deletion burden[21] at recurrence (Fig. 1d, right).

Longitudinal changes in cell-type composition

Global (nonmatched) comparison of cell-type abundance showed overall similarity between time points, except for significantly lower abundance of malignant cells and higher abundance of glio-neural TME (oligodendrocytes, neurons and astrocytes (ACs)) in recurrent tumors (Fig. 2a and Extended Data Fig. 2a). We further separated the broad nonmalignant cell types (for example, myeloid) into more granular

states (for example, microglia and bone marrow-derived macrophages) using non-negative matrix factorization (NMF; Methods). Analysis of these higher-resolution cell states demonstrated that recurrences were enriched with reactive ACs and with oligodendrocytes expressing an interferon program (Extended Data Fig. 2b). To further evaluate differences in cell-type composition, we categorized tumors into six compositional groups based on the relative abundance of malignant and TME cell types (Methods). Briefly, tumors were divided into the following three main groups based on their malignant fraction: high malignant fraction (HMF), intermediate malignant fraction (IMF) and low malignant fraction (LMF). The latter group was further subdivided by the dominant TME cell type (for example, LMF−tumor-associated macrophages (TAM), oligodendrocyte (OC) and glio-neural (GN); Extended Data Fig. 2c, left). The HMF group was enriched in primary tumors, while the LMF with glio-neural (LMF−GN) or oligodendrocytic TME (LMF−OC) were enriched at recurrence ($P = 0.005$ for both groups, two-sided Fisher's test; Fig. 2b, left).

To validate our findings, we re-analyzed an independent longitudinal GBM snRNA-seq cohort[14] (Extended Data Fig. 2d,e). Consistent with our cohort, we observed lower malignant cell abundance, higher oligodendrocyte abundance and similar enrichment of LMF compositional groups at recurrence ($P = 0.04$, two-sided Fisher's exact test; Extended Data Fig. 2f).

Survival analysis stratified by compositional groups showed significant differences in survival time after the second surgery (Extended Data Fig. 2g, top) but not in the time interval between the first and second surgeries. Patients with glio-neural TME at recurrence had significantly longer survival time after second surgery than patients with other recurrences (median = 19 versus 8 months, $P = 0.012$, log-rank test; Fig. 2c, left). These differences in clinical course were independent of other clinical characteristics, including *MGMT* methylation status (Extended Data Fig. 2h, top).

Longitudinal stability of transcriptional features

Next, we investigated changes in malignant cell state abundance across time points. As described in more detail in the companion paper[15], we applied NMF to malignant cells and identified ten GBM metaprograms (MPs) representing intratumoral cellular heterogeneity (Methods)[22–24]. This included the cell cycle and the previously identified AC-like, MES-like, stress, hypoxia, neural progenitor cell-like (NPC-like) and oligodendrocyte progenitor cell-like (OPC-like) states. In addition, we identified the following three previously undescribed states: a differentiated neuronal state (NEU-like), a glial progenitor-like state (GPC-like) and a cilia-related state (Cilia-like), characterized by marker genes, pathway enrichments and similarity with normal neural cell types. Beyond cell states, we defined three baseline gene expression profiles (BP), reflecting intertumor heterogeneity that is not driven by differences in malignant cell state abundance. The three BPs were annotated as glial-BP, ECM-BP and neuronal-BP.

Comparison of malignant cell state abundance between primary and recurrent samples did not reveal significant differences both in our cohort and in the cohort of ref. 14 (Extended Data Fig. 3a,b). Moreover, we did not detect significant differences across time points when considering a division of tumors into six groups based on dominant malignant states or by BPs (Fig. 2b (middle and right), Extended Data Fig. 2c (middle and right) and Extended Data Fig. 3c,d). However, survival analysis stratified by dominant malignant cell states showed significantly worse prognosis in the MES-like/hypoxia group at recurrence (median survival time from second surgery = 5 versus 10.3 months, $P = 0.00086$, log-rank test; Fig. 2c (right) and Extended Data Fig. 2g,h), consistent with a recent study[14].

The multiple transcriptomic layers of cell-type composition, malignant cell states and malignant BPs are significantly associated with each other and define three stereotypical GBM ecosystems (that is, glial, neuronal and ECM)[15]. We next investigated whether interactions
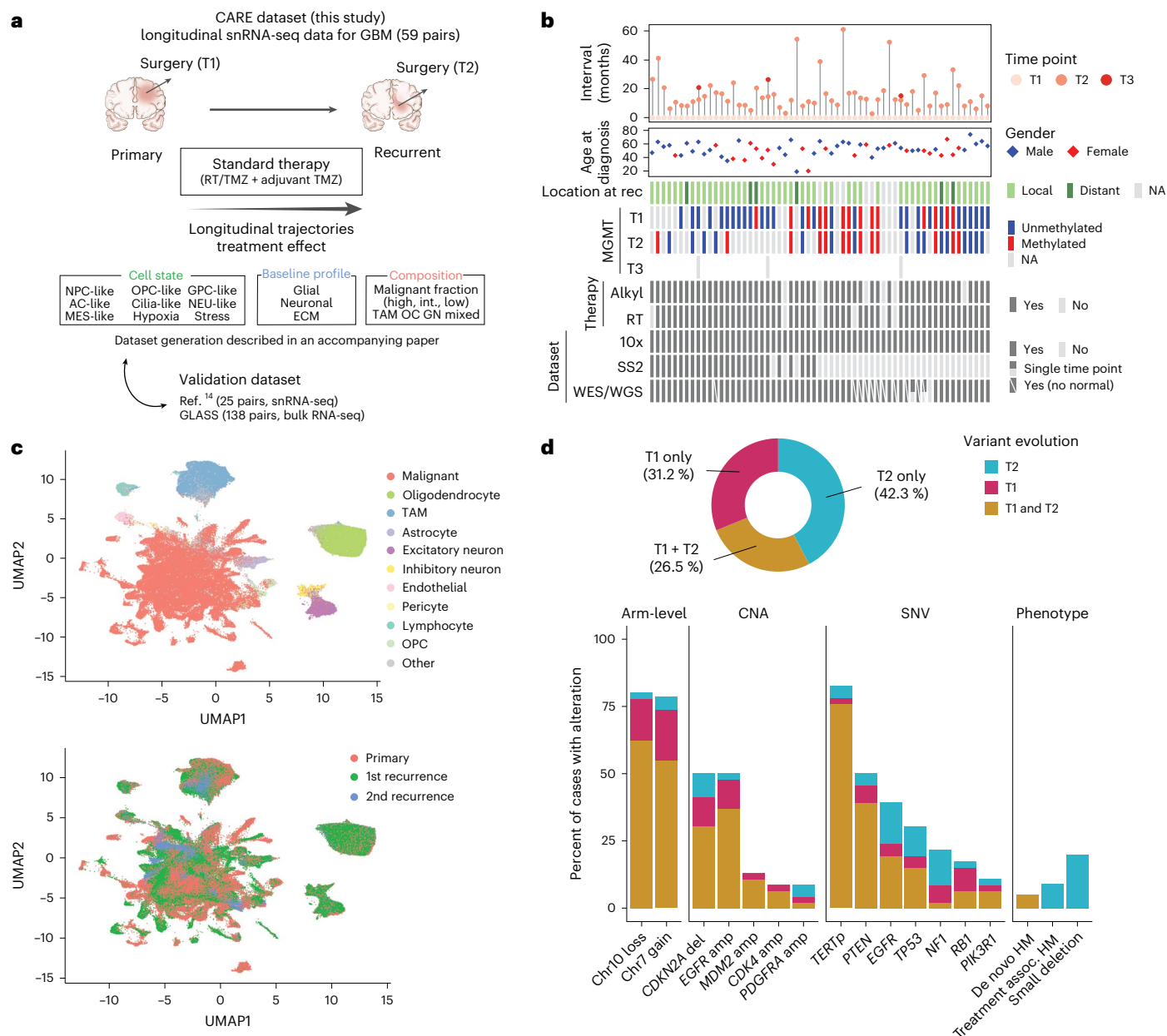
**Fig. 1 | Longitudinal profiling of a clinically annotated GBM cohort.**
a, Schematic representation describing the workflow of our study. TMZ, temozolomide; RT, radiotherapy; int., intermediate. **b**, Clinical and technical information on all 59 patients in this dataset, including surgical interval, age at diagnosis, gender, location at recurrence (rec), *MGMT* promoter status, therapy and omic data type. **c**, UMAP for dimension reduction based on gene expression values of the cells in our cohort colored according to the cell type (top) and time point (bottom). **d**, Proportion (%) of patients in the dataset in which a genetic aberration was detected, colored by time point. The donut chart at the top represents average somatic mutation distribution for whether an alteration was detected at both time points (T1 + T2), the primary tumor only (T1) or the recurrent tumor only (T2). The bar plot at the bottom is for the known driver genomic events and the representative phenotypes related to the genomic alterations—arm-level refers to whole chromosome arm amplification (amp) (chr7q)/deletion (del) (chr10q), CNA refers to high-level gene amplification or deletion, and SNV refers to single-nucleotide mutations. De novo hypermutation (HM) indicates a high mutation burden at both time points without evidence for treatment-associated mutational signatures. Small deletion indicates tumors with increased small deletion burden at recurrence. UMAP, uniform manifold approximation and projection; chr, chromosome; assoc., associated.

between components of the GBM ecosystems are maintained between primary and recurrent tumors. We separately computed for each time point the correlations between (1) proportions of 11 TME cell types, (2) proportions of ten malignant cell states and (3) three BP scores. In both time points, we found three comparable clusters of correlated features (Fig. 2d and Extended Data Fig. 3e). These conserved associations (*P* < 0.01 by permutation test) remain largely stable.

Nevertheless, we did observe some differences, such as preferential association of the neuronal-high ecosystem with OPC-like

malignant cells (in primary samples) and with NEU-like malignant cells (in recurrent samples; Fig. 2d and Extended Data Fig. 3e). Interestingly, ligand–receptor analysis with CellChat[25] showed some differential enrichment of predicted interactions across time points. For example, neuroligin (NLGN) and neuregulin (NRG) gene families—expressed by oligodendrocytes and neurons—are predicted to interact with the neurexin (NRXN) gene family or *ERBB4* on NEU-like and NPC-like malignant cell states, preferentially at recurrence (Extended Data Fig. 3f)[15,26–28]. Taken together, global analysis of our
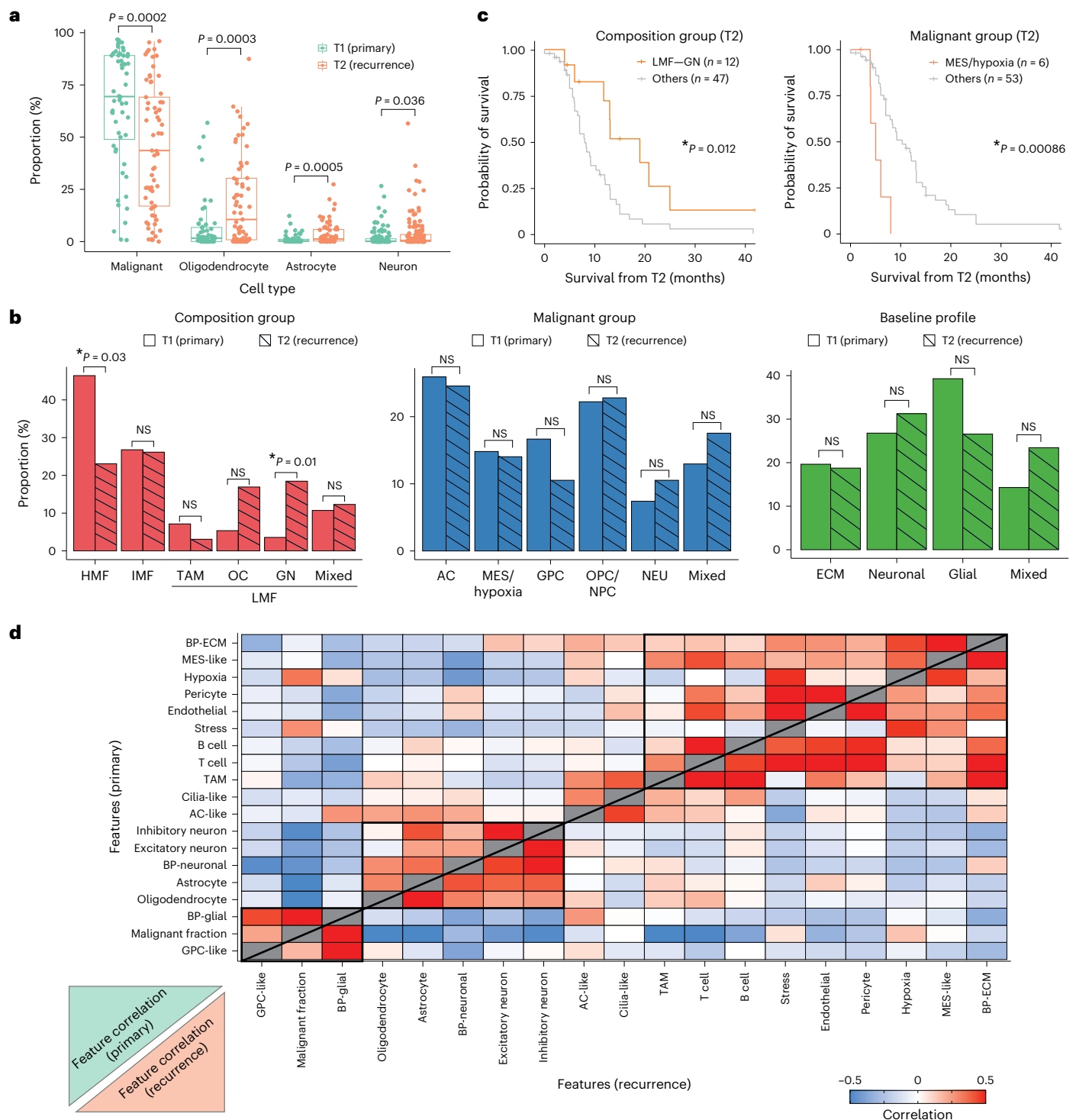
Fig. 2 | Prognostically significant longitudinal cell-type changes in the TME, global similarity of cell states between primary and recurrent tumors.
a, Proportion (%) of each cell type across the two time points (primary and recurrence, *n* = 118) in which a statistically significant difference was observed. *P* values were computed with a two-sided Wilcoxon rank-sum test. **b**, Group-differentiating features and breakdown across primary/recurrence status for composition (left), malignant state frequency (middle) and baseline profiles (right). *P* values were computed using Fisher's exact test. **c**, Kaplan–Meier curves depicting the survival time after the second resection according to the transcriptomic features at the second resection. Left, 12 patients that recurred

with a glio-neural composition group versus 47 patients with other types of recurrences. Right, six patients that recurred with MES/hypoxia cell state group versus 53 patients with other types of recurrences. *X* axis reflects the time from the second resection to outcome. Statistical significance of survival difference between the groups in each panel was computed using the log-rank test.
d, Heatmap showing the Pearson correlation between transcriptomic features. Correlations were computed separately in primary samples (top-left) and in recurrent samples (bottom-right) and are ordered according to the hierarchical clustering pattern of the recurrent samples. NS, not significant.
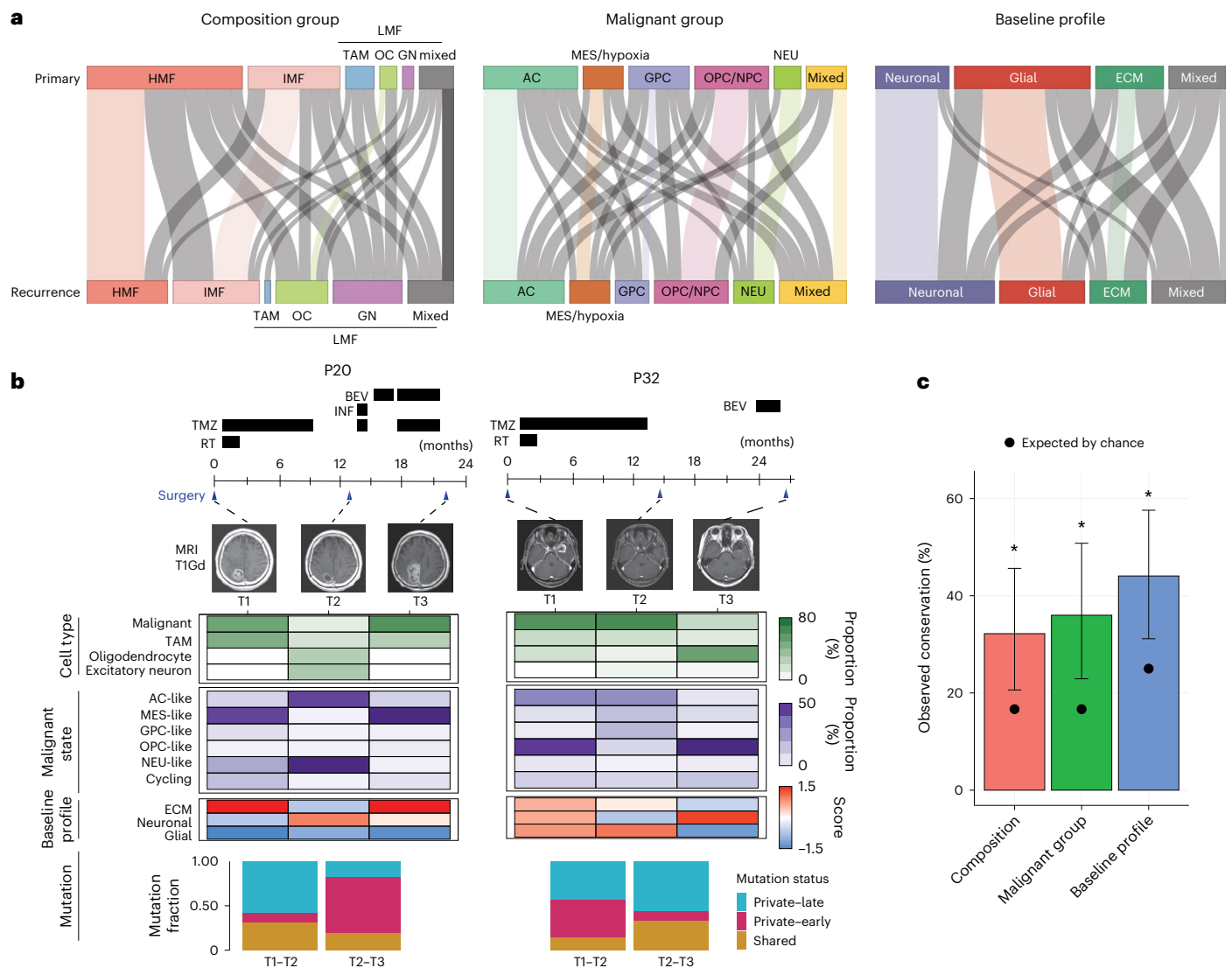
Fig. 3 | Divergence of individual sample pairs. a, Sankey plots depicting the transitions between time points across the composition (left), malignant states (middle) and baseline profile groups (right). The width of the features represents the proportion of tumors with the indicated classification. Light gray links reflect transitions from one group (T1) to a different group at T2. **b**, Longitudinal transcriptomic changes in the two pairs profiled at three time points highlight unpredictable gene expression trajectories. Detailed clinical information including treatment regimen and tumor MRI (top), heatmap representing proportions and scores from three transcriptomic layers (middle) and mutation fraction between time points are shown (bottom). INF, interferon; BEV, bevacizumab; T1Gd, T1-weighted post-gadolinium image. **c**, Observed (colored bar) versus expected (black dot) conservation across time points. *P* values were computed using a binomial test and adjusted for multiple testing using Holm's method. Error bars represent confidence intervals derived from the binomial test. Asterisk indicates a Holm-adjusted *P* < 0.01. MRI, magnetic resonance imaging.

cohort (not matched per sample pairs) shows differences in cell-type composition that are consistent with decreased malignant cell fraction and further integration of recurrent GBM cells with the brain parenchyma[9,29,30], but does not reveal substantial global differences either in malignant cellular states or in BPs.

Divergence of individual sample pairs

Despite global conservation of cell types and malignant cellular states, when examining individual matched sample pairs, we found extensive divergence (Fig. 3a). Most (68%) sample pairs diverged from one compositional group at diagnosis to a different one at recurrence. Similarly, 64% and 56% switched groups of dominant malignant states and of BP, respectively. We observed the same phenomenon in the cohort of ref. 14, with 68% of patients switching compositional groups and 72% switching malignant groups at recurrence (Extended Data Fig. 4a). While no group was significantly enriched, there was a trend toward

increased neuronal-BP and reduced glial-BP at recurrence (Fig. 3a (right)). Remarkably, we observed 72% of all possible trajectories at least once (63 of 88 trajectories), including opposite trajectories. For example, patient P1 had an increase of AC-like and decrease of GPC-like malignant cells at recurrence, while patient P2 had an opposite trajectory (Extended Data Fig. 4b). Furthermore, patients profiled at three time points showed opposite trajectories between two treatment intervals (T1–T2 and T2–T3), despite recurrences occurring at the same site (Fig. 3b). Finally, the frequency of conservation was not significantly different between local and distant recurrences (*P* = 0.66, two-sided Fisher's test).

This divergence of individual sample pairs prompted us to compare the observed patterns of conservation to those expected by a null model in which matched primary–recurrent pairs are as similar to one another as pairs of randomly selected samples. This analysis revealed that, across all three layers, matched pairs were significantly

more conserved than expected by chance ($P < 0.004$ for each layer, binomial test; Fig. 3c). Thus, matched samples usually diverge in their transcriptomic classification and may diverge in a wide range of trajectories between and within patients but remain significantly more likely to retain any specific classification compared to a random pair of samples. This observation prompted us to further stratify our cohorts and attempt to identify predictors/modifiers of evolutionary trajectories.

MGMT expression in GBM single cells influences recurrence trajectories

Previous studies have shown that patients with methylated *MGMT* promoter exhibit better response to TMZ and have more favorable prognosis[2,31], but whether this is mirrored by differences in either cellular architecture or in cellular trajectories following treatment is unknown. We classified patients as methylated (*MGMT*-MET, $n = 12$), unmethylated (*MGMT*-UM, $n = 19$) or unknown ($n = 28$), based on the primary tumor's *MGMT* promoter methylation status. As expected, *MGMT*-MET patients exhibited longer surgical intervals than *MGMT*-UM patients, both in our cohort and in the GLASS cohort (Extended Data Fig. 5a,b).

We next assessed whether *MGMT* promoter methylation status correlated with *MGMT* expression in single cells, as this association has been challenging to establish in bulk analyses[32]. Malignant cell expression of *MGMT* was significantly lower in primary *MGMT*-MET samples than in primary *MGMT*-UM samples ($P = 5.3 \times 10^{-6}$, two-sided Wilcoxon rank-sum test; Fig. 4a)[32,33], but this effect was not observed for TME cell types (Fig. 4b). In a subset of *MGMT*-MET cases, *MGMT* expression increased at recurrence, possibly reflecting a competitive disadvantage of cells with low *MGMT* expression during treatment.

The correlation between *MGMT* promoter methylation and low *MGMT* expression prompted us to build a logistic regression model that uses average malignant cell *MGMT* expression to infer *MGMT* methylation status (Extended Data Fig. 5c). When applying this model, we found that classification by *MGMT* expression levels was associated with surgical resection interval (Fig. 4c) and, in fact, led to improved association compared to classification by *MGMT* promoter methylation alone—within the MGMT-MET group, we observed significantly longer surgical interval for the *MGMT*-low expression group relative to the *MGMT*-high/*MGMT*-intermediate expression groups (Fig. 4d); in contrast, within the MGMT-high expression group, there was no significant difference in surgical interval when further stratifying by *MGMT* promoter methylation status (Fig. 4e). This improved performance of *MGMT* expression level could be due to exclusion of nonmalignant cells that may affect *MGMT* promoter methylation assessment; alternatively, it could indicate that *MGMT* expression level in the therapeutically targeted malignant cells more directly reflects MGMT protein activity and hence is more predictive of treatment response.

Comparison of cellular architecture between *MGMT*-low and *MGMT*-high expression samples showed no significant differences in cell-type composition and malignant state distribution (Extended Data Fig. 5d,e). However, *MGMT* expression level was significantly associated with changes in abundance of MES-like states at recurrence, both in our CARE dataset and in ref. 14 (Fig. 4f and Extended Data Fig. 5f). Specifically, *MGMT*-low tumors recurred with a lower abundance of MES-like states compared to their primary samples, while *MGMT*-high tumors displayed the opposite pattern. Baseline profiles changed in a similar manner—trending toward decreased ECM in *MGMT*-low, highlighting the coordinated evolution of cellular states and BPs (Extended Data Fig. 5g).

To further identify longitudinal gene expression patterns specific to *MGMT*-high and *MGMT*-low samples, we compared their malignant pseudobulk expression (aggregated gene expression from all malignant cells per sample) across time points. This revealed four groups of genes—those consistently upregulated or downregulated in recurrence, regardless of *MGMT* expression (CONS-UP and CONS-DN), and those upregulated specifically in *MGMT*-low (low-UP) or *MGMT*-high samples (high-UP; Extended Data Fig. 5h). CONS-UP was enriched with genes involved in postsynaptic activity (for example, *GRIN1/GRIN2A/GRIN2B*, *GABRA1/GABRA4*), consistent with the trend toward increased neuronal-BP in recurrence (Fig. 3a), while CONS-DN was enriched with genes related to oxidative phosphorylation (for example, *NDUFB4/NDUFB11*, *UQCRB/UQCRQ*) and stemness (for example, *CD24*, *DCX*, *SOX4/SOX11* and *SOX11*; Extended Data Fig. 5i). In contrast to those *MGMT*-independent gene sets, low-UP genes were enriched with genes linked to gliogenesis (for example, *ACSL1*, *OLIG1/OLIG2* and *SOX8*), whereas high-UP genes were enriched with mesenchyme development and ECM remodeling (for example, *COL1A1/COL1A2*, *COL1A2*, *DCN*, *FN1* and *LOXL1*; Fig. 4g). To validate our findings, we repeated this analysis in the ref. 14 dataset and found significant similarities, especially in the high-UP signature (Jaccard index 8.5% versus 1.2% expected, $P < 0.0001$, bootstrapping).

In summary, our single-cell analysis revealed that *MGMT* expression in malignant cells predicts time to recurrence and influences longitudinal cellular trajectories—MES-like state and ECM-related genes tend to be enriched in recurrence in *MGMT*-high (likely nonresponsive) patients, while in *MGMT*-low (likely responsive) patients, recurrence is associated with loss of MES-like states and enrichment of genes related to gliogenesis. Our results suggest that prior attempts that failed at correlating *MGMT* expression with treatment response[32] were likely confounded by bulk analysis and expression of *MGMT* by nonmalignant cells.

Mutational signatures associated with recurrence trajectories

Treatment may affect GBM genetic evolution, as supported by reports of somatic hypermutation following TMZ chemotherapy and/or small deletion phenotype following radiotherapy[7,20,21,34]. To analyze the longitudinal mutation patterns in the CARE cohort, we examined mutation burden and mutational signatures following therapy. We observed that mutation burden (mutations per megabase) generally increased at recurrence ($P = 0.01$, two-sided paired Wilcoxon; Extended Data Fig. 6a) and identified four treatment-associated hypermutant samples (mutation burden > 10 mutations per megabase (Mut per Mb) at recurrence; Methods)[34]. Two tumor pairs displayed high mutation burden at both time points without evidence of treatment-associated mutation signature (COSMIC single base substitution (SBS) 11; Extended Data Fig. 6b).

To investigate new mutational signature associations at recurrence, we examined the frequency of the COSMIC v3 SBS signatures[35], both in our CARE cohort ($n = 46$ patients) and in the GLASS cohort ($n = 138$ patients). In both cohorts, we observed a significant decrease in SBS1 (aging/clock-like etiology) and an increase in SBS21 (defective mismatch repair) at recurrence (Fig. 5a and Extended Data Fig. 6c). Notably, patients with increased mutations attributed to SBS21 did not tend to acquire mutations in mismatch repair genes. While mutational signatures temporally differed, we did not observe individual mutations enriched at recurrence (adjusted Fisher's exact test $P > 0.05$). Among small insertion/deletion variants, we observed increased burden of deletions (Fig. 5b) but not insertions (Extended Data Fig. 5d), including ten recurrences that acquired the small deletion phenotype without treatment-associated hypermutation (Methods; Fig. 5b). Taken together, our analyses reveal that subsets of tumors acquire consistent patterns of genetic alterations following treatment.

To understand whether post-treatment genetic alterations modify cellular state evolution, we investigated the specific trajectories of tumors with hypermutation, SBS21, and small deletion phenotypes. For hypermutant tumors, we did not observe a consistent cellular phenotype at recurrence, although this analysis was limited by sample size ($n = 4$). In contrast, patients who acquired small deletions were enriched with hypoxia and MES-like cell states (Fig. 5c and Extended Data Fig. 6e; paired Wilcoxon rank-sum test, $P < 0.05$). We observed a
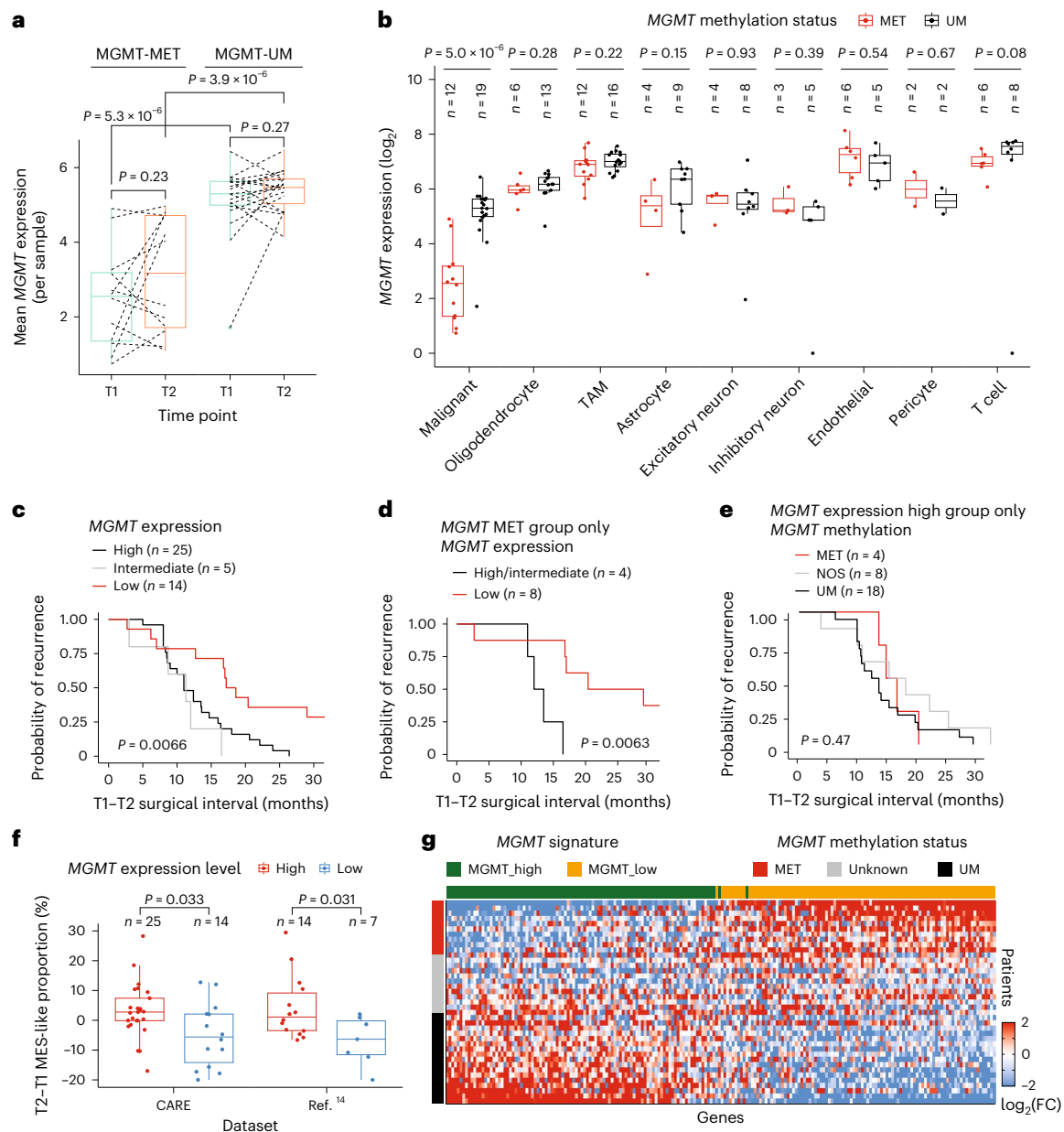
Fig. 4 | *MGMT* expression in GBM single cells influences recurrence trajectories. a, Average *MGMT* expression in malignant cells per sample across time points. Samples were included only if the *MGMT* promoter status was verified using a methylation assay and were annotated as methylated/unmethylated according to the status of the primary sample (*n* = 12 methylated and *n* = 19 unmethylated). Dashed lines connect matched samples. Statistical significance was estimated using a two-sided Wilcoxon rank-sum test; unadjusted *P* values are shown. In **a**, for within-group comparisons, a Wilcoxon signed rank test (paired) was used. **b**, *MGMT* expression level in each cell type between methylated and unmethylated samples. Statistical significance was estimated using a two-sided Wilcoxon rank-sum test; unadjusted *P* values are shown. **c**, Survival curve for the patients included in this analysis stratified according to *MGMT* expression level. *X* axis reflects the time from first to second resection. Statistical significance of survival difference between the groups in each panel was computed using the log-rank test. **d**, Survival curves for *MGMT*-MET patients stratified according to *MGMT* expression level. *X* axis reflects the time from first

to second resection. Statistical significance of survival difference between the groups in each panel was computed using the log-rank test. **e**, Survival curves for *MGMT* expression high group stratified according to *MGMT* promoter methylation status. *X* axis reflects the time from first to second resection. Statistical significance of survival difference between the groups in each panel was computed using the log-rank test. NOS, not otherwise specified. **f**, Difference in MES-like cell state proportion (%) across the two time points (primary and recurrence) stratified by *MGMT* expression level in this study and in ref. 14. All sample points are shown as jittered points. Statistical significance was estimated using a two-sided Wilcoxon rank-sum test; unadjusted *P* values are shown. **g**, *MGMT*-specific signatures plotted for patients included in the analysis. Value represents the T2–T1 difference (log₂(FC)) of gene expression for each patient. Patients are ordered according to the difference between signature scores. Genes are ordered according to their correlation (across patients) with the difference between signature scores. FC, fold change.

similar effect for tumors with increased SBS21 signal, although this effect was weaker when excluding samples with co-occurring small deletion phenotype (Fig. 5c and Extended Data Fig. 6f). The association between recurrence-specific small deletions and hypoxia state

was recapitulated in analysis of bulk samples from GLASS[9] (Fig. 5d). In contrast, the MES-like observation did not validate in the GLASS cohort (Extended Data Fig. 6g), possibly due to similarities between MES-like and nonmalignant profiles that make it difficult to disentangle these
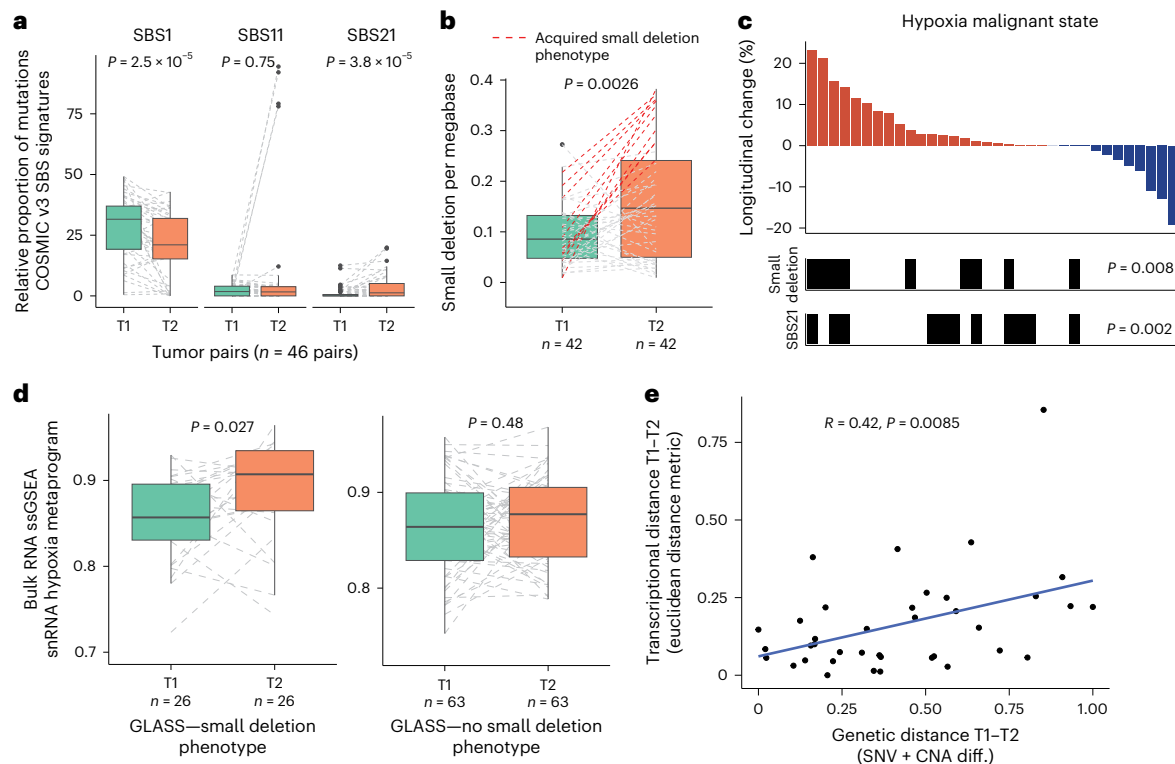
Fig. 5 | Mutational signatures associated with recurrence trajectories.
a, Longitudinal difference in the relative proportion of mutations assigned to
COSMIC v3 mutational signatures at each time point for select SBS signatures
(SBS1, clock-like; SBS11, alkylating agent; and SBS21, defective DNA mismatch
repair). Outlier points are shown. Dashed lines connect values from the same
patient at T1 and T2. *P* values represent two-sided paired Wilcoxon rank-sum
test. **b**, Longitudinal difference in small deletion burden between T1 and T2 with
dashed lines connecting patient values and red indicating patients who were
assigned to the increased small deletion burden group. Analysis restricted to
nonhypermutant cases. *P* values reflect two-sided paired Wilcoxon rank-sum
test. **c**, A waterfall plot of the relative change in hypoxia-related malignant state
sorted by decreasing longitudinal change. Patients are represented by a single
bar (*x* axis). Presence of increased small deletion burden or SBS21 signature is
presented in black annotation bars below. The reported *P* values indicate

two-sided paired Wilcoxon rank-sum test for the longitudinal change in the
hypoxia malignant state for those patients with small deletion or SBS21 increase.
d, Bulk RNA data from the GLASS consortium were scored for the hypoxia snRNA
malignant metaprogram signature and the relative ssGSEA score is presented
on the *y* axis. The panels show the longitudinal change in the hypoxia signature
for those patients whose tumor had a small deletion increase (left) and for those
that did not have small deletion burden increase (right). *P* values from two-sided
paired Wilcoxon rank-sum test. **e**, Scatterplot that represents the scaled genetic
distance (bulk DNA—proportions of private mutations and differences in copy-
number altered regions) versus scaled transcriptional distance (snRNA), with the
linear regression line shown in blue. The Pearson's correlation coefficient and
associated *P* value are shown (*n* = 38). ssGSEA, single-sample gene set enrichment
analysis; diff., differences.

signals in bulk datasets. Hypoxic cells have been linked to deregulated
epigenetics and stress responses[36] and, consequently, to increased
resistance to radiation[37]. Thus, malignant cells in hypoxic regions may
be better able to repair radiotherapy-associated DNA damage, leading
to an outgrowth of hypoxic state at recurrence.

Finally, we examined the correlation between overall genetic
distance, as defined by longitudinal single-nucleotide variant (SNV)/
CNA differences, and overall malignant transcriptional distance (Meth-
ods). We found a significant correlation (Pearson's correlation = 0.42,
P = 0.009; Fig. 5e) that was retained when analyzing only SNV or CNAs
(Extended Data Fig. 6h,i), suggesting that intratumoral genetic evo-
lution during disease progression contributes to transcriptional
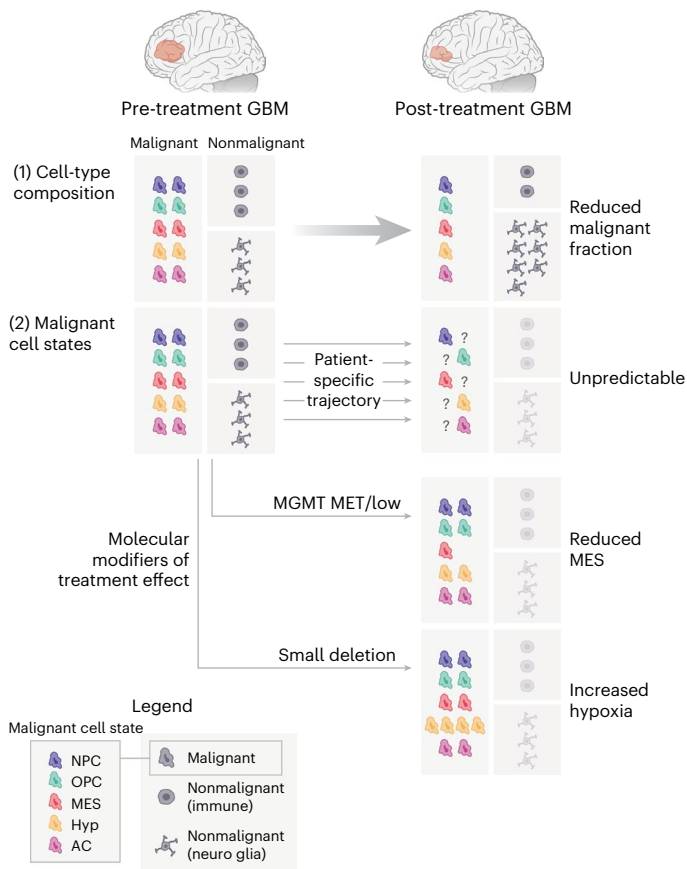evolution.

Discussion

Intertumoral and intratumoral heterogeneity in GBM has been asso-
ciated with treatment resistance and disease recurrence, but how
specific subsets of GBM cells respond to therapy remains poorly
understood. Here we leveraged a longitudinally matched multi-omic
GBM snRNA-seq and bulk DNA dataset of 121 tumors from 59 patients
consisting of ~430,000 nuclei to comprehensively characterize the
compositional, transcriptional and genetic changes that GBMs undergo

following standard-of-care. We found extensive variability in longitu-
dinal trajectories of different patients (Fig. 6). While many trajectories
were unpredictable, we identified patient characteristics—*MGMT* meth-
ylation and increased small deletion burden—that were associated with
particular trajectories and expanded our understanding of recurrences.

Previous studies have highlighted specific transcriptional tra-
jectories during GBM evolution. The recent GLASS consortium study
highlighted three trajectories toward neuronal, MES and prolifera-
tive profiles[9], and other studies have highlighted proneural-to-MES
phenotypic shifts[11,14,38]. While we similarly identified these
recurrence-associated patterns, our analysis suggests that their over-
all frequency is limited and that such trajectories are enriched only
in specific subsets of patients, while global comparison of cell states
between primary and recurrent samples shows overall similarity. In
particular, a shift toward the MES phenotype following treatment was
not observed as a globally enriched trend in our dataset, only in specific
subsets of patients. This discordance with prior studies may be attribut-
able to at least the following three effects: (1) differences in technology
(for example, bulk versus single-cell profiling), (2) cohort/sampling
(for example, single-center sampling, tissue digestion versus not) and
(3) analysis methods. There may also be biases due to additional treat-
ments that were not addressed (bevacizumab, corticosteroids, etc.).

Fig. 6 | Longitudinal GBM cell state trajectories. Analysis of the GBM CARE dataset reveals key patterns of GBM evolution following treatment. (1) The most common observation was in the cell-type composition layer, where many samples exhibited a reduced malignant cell fraction at recurrence. (2) At the malignant state level, many tumors recurred with an unpredictable trajectory that likely reflects patient-specific evolution (top). A smaller subset of tumors recurred with more predictable trajectories, such as reduced MES-like fraction for *MGMT*-MET versus *MGMT*-UM primary tumors (middle) or increased hypoxia fraction for samples with increased small deletion burden following treatment (bottom). Columns separated into malignant and nonmalignant fractions indicate the relative proportions per tumor. Only selected nonmalignant and malignant cell states are shown for clarity. Hyp, hypoxia.

NEU-like malignant state and the neuronal baseline expression profile of the tumors. These results suggest that, following treatment, integration of the residual GBM cells with the brain parenchyma is likely enhanced[29,30].

Beyond defined subsets, our study makes the challenging observation that, for the majority of GBMs, longitudinal cellular trajectories are diverse and unpredictable. We speculate that this diversity reflects at least the following three phenomena: first, given the genetic and epigenetic heterogeneity in primary tumors, it might be expected that tumors with distinct underlying biology will also have distinct trajectories of recurrence. Second, even within a single GBM, there is extensive spatial heterogeneity[23,40]; as primary and recurrent samples are obtained from different locations, their differences might reflect such spatial heterogeneity and, therefore, depend on sampling[40]. Third, patients vary considerably both in their treatment histories and in their response to treatments, potentially leading to distinct recurrence trajectories. Many GBM patients are treated by additional therapies in diverse combinations beyond standard-of-care, which is a limitation in this study. Moreover, even standard-of-care induces distinct patient responses, and we identified the following two cases in which treatment responses are linked to recurrence trajectory: (1) MGMT-MET (MGMT-low expression) samples (more likely to respond to alkylating agents) are associated with depletion of MES-like states in recurrence and (2) the small deletion phenotype, previously linked to radiotherapy[21], is associated with increased hypoxia states in recurrence.

In summary, we present a comprehensive analysis of GBM recurrence at single-cell resolution. Our analysis shows that, globally, recurrent GBMs are generally similar to primary GBMs in their cellular states, composition and other features of the GBM ecosystem. Accordingly, a wide range of recurrence trajectories are observed, highlighting extensive diversity in GBM evolution. Nevertheless, subsets of tumors with evidence for particular treatment responses are skewed toward specific transcriptional trajectories. These findings offer more detailed insights over prior observations and provide an opportunity to stratify recurrent patients more precisely, potentially leading to specific treatment strategies.

Online content

Any methods, additional references, Nature Portfolio reporting summaries, source data, extended data, supplementary information, acknowledgements, peer review information; details of author contributions and competing interests; and statements of data and code availability are available at https://doi.org/10.1038/s41588-025-02168-4.

Our dataset contains tumor samples that were collected from seven medical centers across six countries, limiting the possibility of results being skewed toward a particular recurrence trajectory due to institution-specific procedures. Moreover, the samples in our dataset were processed and profiled by three different labs, limiting the possibility of skewing due to a lab-specific batch effect. The snRNA-seq protocol used by our labs to process and profile tumor samples was digestion-independent and optimized for brain tumors[39], capturing a higher number of transcripts than prior single-nucleus GBM studies (Extended Data Fig. 2e). This likely results in a more faithful representation of the tumor tissue, as evident by the higher diversity of TME cell types in our dataset and the discovery of new malignant cell states.

Neuronal pathways were consistently found to be upregulated in recurrent GBM[8,9,12]. However, it is important to note that this reflects only subsets of patients in each study and that we observe a wide diversity of trajectories from primary to matched recurrent samples. Leveraging the resolution and scale of our dataset, we showed that this phenomenon correlates with decreased malignant cell fraction and concomitant increased proportions of neurons in the TME; only in a small subset of cases, this is accompanied by the enrichment of

References

1. Louis, D. N. et al. The 2021 WHO classification of tumors of the central nervous system: a summary. *Neuro Oncol.* **23**, 1231–1251 (2021).
2. Hegi, M. E. et al. Gene silencing and benefit from temozolomide in glioblastoma. *N. Engl. J. Med.* **352**, 997–1003 (2005).
3. Stupp, R. et al. Radiotherapy plus concomitant and adjuvant temozolomide for glioblastoma. *N. Engl. J. Med.* **352**, 987–996 (2005).
4. Mu, Q. et al. Identifying predictors of glioma evolution from longitudinal sequencing. *Sci. Transl. Med.* **15**, eadh4181 (2023).
5. Kim, J., Lee, I., Cho, H. J., Lee, J. & Park, P. J. Spatiotemporal evolution of the primary glioblastoma genome article spatiotemporal evolution of the primary glioblastoma genome. *Cancer Cell* **28**, 318–328 (2015).
6. Kim, H. et al. Whole-genome and multisector exome sequencing of primary and post-treatment glioblastoma reveals patterns of tumor evolution. *Genome Res.* **25**, 316–327 (2015).
7. Barthel, F. P. et al. Longitudinal molecular trajectories of diffuse glioma in adults. *Nature* **576**, 112–120 (2019).

8. Kim, K. et al. Integrated proteogenomic characterization of glioblastoma evolution. *Cancer Cell* **42**, 358–377 (2024).

9. Varn, F. S. et al. Glioma progression is shaped by genetic evolution and microenvironment interactions. *Cell* **185**, 2184–2199.e16 (2022).

10. Hoogstrate, Y. et al. Transcriptome analysis reveals tumor microenvironment changes in glioblastoma. *Cancer Cell* **41**, 678–692 (2023).

11. Wang, J. et al. Clonal evolution of glioblastoma under therapy. *Nat. Genet.* **48**, 768–776 (2016).

12. Garofano, L. et al. Pathway-based classification of glioblastoma uncovers a mitochondrial subtype with therapeutic vulnerabilities. *Nat. Cancer* **2**, 141–156 (2021).

13. Wang, L. et al. The phenotypes of proliferating glioblastoma cells reside on a single axis of variation. *Cancer Discov.* **9**, 1708–1719 (2019).

14. Wang, L. et al. A single-cell atlas of glioblastoma evolution under therapy reveals cell-intrinsic and cell-extrinsic therapeutic targets. *Nat. Cancer* **3**, 1534–1552 (2022).

15. Nomura, M. et al. The multilayered transcriptional architecture of glioblastoma ecosystems. *Nat. Genet.* https://doi.org/10.1038/s41588-025-02167-5 (2025).

16. Campbell, J. N. et al. A molecular census of arcuate hypothalamus and median eminence cell types. *Nat. Neurosci.* **20**, 484–496 (2017).

17. Habib, N. et al. Div-Seq: single-nucleus RNA-seq reveals dynamics of rare adult newborn neurons. *Science* **353**, 925–928 (2016).

18. Polioudakis, D. et al. A single-cell transcriptomic atlas of human neocortical development during mid-gestation. *Neuron* **103**, 785–801.e8 (2019).

19. Nowakowski, T. J. et al. Spatiotemporal gene expression trajectories reveal developmental hierarchies of the human cortex. *Science* **358**, 1318–1323 (2017).

20. Johnson, B. E. et al. Mutational analysis reveals the origin and therapy-driven evolution of recurrent glioma. *Science* **343**, 189–193 (2014).

21. Kocakavuk, E. et al. Radiotherapy is associated with a deletion signature that contributes to poor outcomes in patients with cancer. *Nat. Genet.* **53**, 1088–1096 (2021).

22. Kinker, G. S. et al. Pan-cancer single-cell RNA-seq identifies recurring programs of cellular heterogeneity. *Nat. Genet.* **52**, 1208–1218 (2020).

23. Greenwald, A. C. et al. Integrative spatial analysis reveals a multi-layered organization of glioblastoma. *Cell* **187**, 2485–2501.e26 (2024).

24. Gavish, A. et al. Hallmarks of transcriptional intratumour heterogeneity across a thousand tumours. *Nature* **618**, 598–606 (2023).

25. Jin, S. et al. Inference and analysis of cell–cell communication using CellChat. *Nat. Commun.* **12**, 1088 (2021).

26. Gjørlund, M. D. et al. Neuroligin-1 induces neurite outgrowth through interaction with neurexin-1β and activation of fibroblast growth factor receptor-1. *FASEB J.* **26**, 4174–4186 (2012).

27. Venkatesh, H. S. et al. Targeting neuronal activity-regulated neuroligin-3 dependency in high-grade glioma. *Nature* **549**, 533–537 (2017).

28. Müller, T. et al. Neuregulin 3 promotes excitatory synapse formation on hippocampal interneurons. *EMBO J.* **37**, e98858 (2018).

29. Venkatesh, S. et al. Electrical and synaptic integration of glioma into neural circuits. *Nature* **573**, 539–545 (2019).

30. Venkataramani, V. et al. Glioblastoma hijacks neuronal mechanisms for brain invasion. *Cell* **185**, 2899–2917.e31 (2022).

31. Rivera, A. L. et al. MGMT promoter methylation is predictive of response to radiotherapy and prognostic in the absence of adjuvant alkylating chemotherapy for glioblastoma. *Neuro Oncol.* **12**, 116–121 (2010).

32. Butler, M. et al. MGMT status as a clinical biomarker in glioblastoma. *Trends Cancer* **6**, 380–391 (2020).

33. Costello, J. F., Futsched, B. W., Tanoil, K., Graunkes, D. M. & Pieper, R. Graded methylation in the promoter and body of the 06-methylguanine DNA methyltransferase (*MGMT*) gene correlates with MGMT expression in human glioma cells. *J. Biol. Chem.* **269**, 17228–17237 (1994).

34. Touat, M. et al. Mechanisms and therapeutic implications of hypermutation in gliomas. *Nature* **580**, 517–523 (2020).

35. Alexandrov, L. B., Kim, J., Haradhvala, N. J. & Huang, M. N. The repertoire of mutational signatures in human cancer. *Nature* **578**, 94–101 (2020).

36. Johnson, K. C. et al. Single-cell multimodal glioma analyses identify epigenetic regulators of cellular plasticity and environmental stress response. *Nat. Genet.* **53**, 1456–1468 (2021).

37. Telarovic, I., Wenger, R. H. & Pruschy, M. Interfering with tumor hypoxia for radiotherapy optimization. *J. Exp. Clin. Cancer Res.* **40**, 197 (2021).

38. Wang, Q. et al. Tumor evolution of glioma-intrinsic gene expression subtypes associates with immunological changes in the microenvironment. *Cancer Cell* **32**, 42–56.e6 (2017).

39. Slyper, M. et al. A single-cell and single-nucleus RNA-seq toolbox for fresh and frozen human tumors. *Nat. Med.* **26**, 792–802 (2020).

40. Mathur, R. et al. Glioblastoma evolution and heterogeneity from a 3D whole-tumor perspective. *Cell* **187**, 446–463.e16 (2024).

Avishay Spitzer[1,2,3,39], Kevin C. Johnson [4,39], Masashi Nomura [5,6,7,39], Luciano Garofano [8,9,39], Djamel Nehar-belaid [10], Noam Galili Darnell [1], Alissa C. Greenwald[1], Lillian Bussema [5,6], Young Taek Oh[9], Frederick S. Varn [10,11,12], Fulvio D'Angelo [9,13], Simon Gritsch[5,6,14], Kevin J. Anderson [10], Simona Migliozzi[9,15], L. Nicolas Gonzalez Castro [5,6,16,17], Tamrin Chowdhury[4], Nicolas Robine [18], Catherine Reeves [19], Jong Bae Park [20], Anuja Lipsa[21], Frank Hertel[21], Anna Golebiewska [21], Simone P. Niclou [21,22], Labeeba Nusrat[23], Sorcha Kellet[23], Sunit Das[23], Hyo-Eun Moon[24], Sun Ha Paek [24,25], Franck Bielle [26,27], Alice Laurenge [26,28], Anna Luisa Di Stefano [29,30], Bertrand Mathon [31],

Alberto Picca[26,28], **Marc Sanson**[26,28,32], **Shota Tanaka**[7], **Nobuhito Saito**[7], **David M. Ashley** ◉ [33], **Stephen T. Keir**[33], **Keith L. Ligon** ◉ [34,35], **Jason T. Huse** ◉ [36], **W. K. Alfred Yung** ◉ [37], **Anna Lasorella** ◉ [9,15,40] ✉, **Antonio Iavarone** ◉ [9,13,40] ✉, **Roel G. W. Verhaak** ◉ [4,38,40] ✉, **Itay Tirosh** ◉ [1,40] ✉ & **Mario L. Suvà** ◉ [5,6,40] ✉

[1]Department of Molecular Cell Biology, Weizmann Institute of Science, Rehovot, Israel. [2]Department of Oncology, Tel Aviv Sourasky Medical Center, Tel Aviv, Israel. [3]Faculty of Medicine, Tel Aviv University, Tel Aviv, Israel. [4]Department of Neurosurgery, Yale School of Medicine, New Haven, CT, USA. [5]Department of Pathology and Krantz Family Center for Cancer Research, Massachusetts General Hospital and Harvard Medical School, Boston, MA, USA. [6]Broad Institute of Harvard and MIT, Cambridge, MA, USA. [7]Department of Neurosurgery, Graduate School of Medicine, The University of Tokyo, Tokyo, Japan. [8]Department of Public Health Sciences, Division of Biostatistics and Bioinformatics, University of Miami, Miller School of Medicine, Miami, FL, USA. [9]Sylvester Comprehensive Cancer Center, University of Miami, Miller School of Medicine, Miami, FL, USA. [10]The Jackson Laboratory for Genomic Medicine, Farmington, CT, USA. [11]Department of Genetics and Genome Sciences, University of Connecticut Health Center, Farmington, CT, USA. [12]Institute for Systems Genomics, University of Connecticut, Storrs, CT, USA. [13]Department of Neurological Surgery, University of Miami, Miller School of Medicine, Miami, FL, USA. [14]Department of Neurology, Massachusetts General Hospital and Harvard Medical School, Boston, MA, USA. [15]Department of Biochemistry and Molecular Biology, University of Miami, Miller School of Medicine, Miami, FL, USA. [16]Department of Neurology, Brigham and Women's Hospital, Harvard Medical School, Boston, MA, USA. [17]Center for Neuro-Oncology, Dana-Farber Cancer Institute, Harvard Medical School, Boston, MA, USA. [18]Department of Computational Biology, New York Genome Center, New York City, NY, USA. [19]Department of Sequencing Operations, New York Genome Center, New York City, NY, USA. [20]Department of Cancer Biomedical Science, Graduate School of Cancer Science and Policy, National Cancer Center, Goyang, Republic of Korea. [21]NORLUX Neuro-Oncology Laboratory, Department of Cancer Research, Luxembourg Institute of Health, Luxembourg, Luxembourg. [22]University of Luxembourg Faculty of Science, Technology and Medicine, Luxembourg, Luxembourg. [23]Division of Neurosurgery, St. Michael's Hospital, University of Toronto, Toronto, Ontario, Canada. [24]Department of Neurosurgery, Cancer Research Institute, Hypoxia/Ischemia Disease Institute, Seoul National University, Seoul, Republic of Korea. [25]Advanced Institutes of Convergence Technology, Seoul National University, Suwon-si, Republic of Korea. [26]Sorbonne Université, UMR S 1127, Inserm U 1127, CNRS UMR 7225, ICM—Paris Brain Institute, Equipe labellisée LNCC, Paris, France. [27]AP-HP, Groupe Hospitalier Pitié-Salpêtrière, Neuropathology, Paris, France. [28]AP-HP, Groupe Hospitalier Pitié-Salpêtrière, Neuro-oncology, Paris, France. [29]Neurology Department, Foch Hospital, Suresnes, France. [30]Neurosurgery Unit, Ospedali Riuniti di Livorno, Livorno, Italy. [31]AP-HP, Groupe Hospitalier Pitié-Salpêtrière, Neurosurgery, Paris, France. [32]Brain Tumor Bank Onconeurotek (ONT), AP-HP, Paris, France. [33]Department of Neurosurgery, The Preston Robert Tisch Brain Tumor Center, Duke University, Durham, NC, USA. [34]Department of Pathology, Brigham and Women's Hospital, Boston, MA, USA. [35]Department of Pathology, Dana–Farber Cancer Institute, Boston, MA, USA. [36]Department of Pathology, The University of Texas MD Anderson Cancer Center, Houston, TX, USA. [37]Department of Neuro-Oncology, The University of Texas MD Anderson Cancer Center, Houston, TX, USA. [38]Department of Neurosurgery, Amsterdam University Medical Center, Amsterdam, the Netherlands. [39]These authors contributed equally: Avishay Spitzer, Kevin C. Johnson, Masashi Nomura, Luciano Garofano. [40]These authors jointly supervised this work: Anna Lasorella, Antonio Iavarone, Roel G. W. Verhaak, Itay Tirosh, Mario L. Suvà. ✉e-mail: axl4252@med.miami.edu; axi435@med.miami.edu; roel.verhaak@yale.edu; Itay.tirosh@weizmann.ac.il; suva.mario@mgh.harvard.edu

Methods

Experimental method details

Human participants and ethical approval. Frozen GBM specimens that were diagnosed as 'glioblastoma, IDH-wildtype' according to the World Health Organization 2021 classification were collected at seven institutions, listed below. Collection and genomic profiling were approved by the institutional review board of each institution, and all patients provided informed consent accordingly. The tumors were collected from the MD Anderson Cancer Center, approved by the Institutional Review Board of MD Anderson Cancer Center under the protocol 2012-0441. Duke University cohort ($n = 12$)—the tumors were collected from the Preston Robert Tisch Brain Tumor Center Biorepository, Duke University Hospital. It was approved by the Institutional Review Board of Duke University under the protocol Pro0007434. Tokyo University cohort ($n = 30$)—the tumors were collected from the Department of Neurosurgery, Tokyo University Hospital. It was approved by the Institutional Review Board of Tokyo University Hospital under the protocol G10028. Pitié-Salpêtrière Hospital cohort ($n = 28$)—the tumors were collected from Pitié-Salpêtrière Hospital. It was approved by the Onconeurotek Brain Tumor Bank of the hospital Pitié-Salpêtrière certification 96-900. St. Michael's Hospital cohort ($n = 14$)—the tumors were collected from the Division of Neurosurgery, St. Michael's Hospital, Unity Health Toronto. It was approved by the Research Ethics Board of St. Michael's Hospital, Unity Health Toronto, under the protocol REB 13-141, and all patients provided signed informed consent accordingly. Seoul National University (SNU) cohort ($n = 20$)—the tumors were collected from the Department of Neurosurgery, SNU Hospital. It was approved by the Institutional Review Board of SNU Hospital (approval H-2004-049-1116). NORLUX Neuro-oncology Laboratory (NORLUX) cohort ($n = 13$)—the tumors were collected from Centre Hospitalier de Luxembourg (CHL, Neurosurgical Department). It was approved by the National Committee for Ethics in Research, Luxembourg, under the protocol 201201/06. Cohorts were added to the Institutional Review Board protocol Dana–Farber/Harvard Cancer Center 10-417. Patients were male and female. Clinical information of the cohorts is summarized in Supplementary Table 1.

Statistics and reproducibility. No statistical method was used to determine the sample size. Data were excluded from select analyses when the number of malignant cells within a sample was low in at least one time point. Throughout the figures in this manuscript (Figs. 2–5 and Extended Data Figs. 1–3, 5 and 6), the boxplots reflect the following summary statistics: (1) the line splitting the box represents the median value; (2) the lower and upper edges correspond to the first and third quartiles (the 25th and 75th percentiles); (3) the upper whisker extends from the edge to the largest value no further than 1.5× interquartile range (IQR) from the edge; (4) the lower whisker extends from the edge to the smallest value at most 1.5× IQR of the edge; and (5) if the plots do not include jitter points representing the actual data, then data beyond the end of the whiskers are plotted individually as outlying points. The statistical analysis described in this work was done using R version 4.0.1 and above.

Nuclei isolation from frozen tissue. Protocol 1 (laboratory 1 and laboratory 2 for the cohorts from Duke University, MD Anderson Cancer Center, Tokyo University Hospital, St. Michael's Hospital and Pitié-Salpêtrière Hospital)—nuclei from frozen tumor tissue were isolated as follows: tissue was thawed and mechanically dissociated in salt-Tris buffer (10 mM Tris–HCl (pH 7.5), 146 mM NaCl, 1 mM CaCl$_2$ and 21 mM MgCl$_2$) with 0.49% CHAPS (3-((3-cholamidopropyl) dimethylammonio)-1-propanesulfonate) (Millipore, 28300). Single-nuclei suspensions were filtered using a 40 µm strainer, centrifuged at 500g for 5 min and resuspended in salt-Tris buffer supplemented with 0.01% BSA (NEB, B9000S). Nuclear suspensions were

inspected by microscope, counted using a hemocytometer and used for 10x Genomics workflow.

Protocol 2 (laboratory 3 for the cohorts from NORLUX and SNU cohorts)—tissue samples were thawed and mechanically dissociated in nuclei EZ lysis buffer (Millipore Sigma, NUC101) via Dounce homogenization. The solutions were incubated on ice for 5 min and mixed one to two times during incubation. Single-nuclei suspensions were filtered through a 70 µm strainer and centrifuged at 500g for 5 min at 4 °C, resuspended in nuclei EZ lysis buffer and incubated on ice for 5 min. The solutions were centrifuged at 500g for 5 min at 4 °C and resuspended in 1% BSA/0.2 U µl RNase inhibitor/PBS buffer (three times). For the final resuspension, the DAPI was added to the buffer, the solution was filtered through a 40 µm strainer, cells were counted on a Countess II automated cell counter (Thermo Fisher Scientific) and nuclei were taken into the 10x Genomics workflow.

10x Genomics for single-nucleus sequencing. The 10x Chromium Single Cell 3′ Reagent Kit v3 (10x Genomics, PN1000128) was used according to the manufacturer's protocol. In brief, nuclei were loaded on the Chromium Chip (10x Genomics, PN12000120) with a target cell recovery of 6,000–8,000 nuclei and processed in the Chromium Controller. Single nuclei were partitioned into gel beads-in-emulsion (GEMs), followed by RNA reverse transcription with barcoding. Libraries were created by breaking GEMs and pooling barcoded fractions, cDNA amplification, fragmentation and attachment of sample index and adapter and sequenced on NextSeq500 or NovaSeq (Illumina). For NORLUX and SNU cohorts, nuclei were loaded on a Chromium chip with a target cell recovery of 6,000 nuclei for single-cell multiome ATAC and gene expression according to the manufacturer's protocol. The gene expression chemistry for the 10x multiome possesses the same chemistry as the 10x v3 3′ snRNA-seq.

WES. WES for the samples from Duke University, MDACC, Tokyo University Hospital and St. Michael's Hospital was performed as follows: DNA was extracted from each frozen tumor sample and blood sample corresponding to the patients using the DNeasy Blood & Tissue kit (Qiagen, 69504). The genomic DNA (100–250 ng) was acoustically sheared by an ultrasonicator (Covaris), targeting 150 bp fragments. Library preparation was performed by KAPA HyperPrep Kit (KAPA Biosystems, KK8504) followed by the enzymatic clean-up using AMPure XP beads (Beckman Coulter, A63882). Exome capture was performed using a custom exome bait (manufactured by Twist Biosciences to Broad Institute's specification). Captured libraries were sequenced with 150-base-pair paired-end sequencing on a NovaSeq 6000 (Illumina). For the samples from Pitié-Salpêtrière Hospital, after the DNA was fragmented by a LE220 ultrasonicator (Covaris) and size selected, library preparation and capture were performed using the Twist Human Core Exome kit (Twist Bioscience) according to the manufacturer's protocol. Sequencing was performed on a NovaSeq 6000 (Illumina) with 200-base-pair paired-end sequencing.

WGS. Newly generated whole-genome DNA-sequencing data were collected for a cohort of frozen samples from the NORLUX Neuro-oncology Laboratory. Briefly, DNA was extracted from each tumor sample using the AllPrep DNA/RNA Minikit (Qiagen, 80204) for samples with sufficient tumor tissue and matched normal blood when it was available. Note that the selected tissue for bulk DNA isolation was adjacent to the tissue used for single-nuclei data generation. Briefly, DNA was sheared to 400 bp using a LE220 ultrasonicator (Covaris) and size-selected using AMPure XP beads (Beckman Coulter, A63882). Whole-genome libraries were prepared and sequenced with 150-base-pair paired-end sequencing on a NovaSeq 6000 (Illumina). WGS data for the SNU cohort were prepared identically and were previously reported in ref. 9. Data for the SNU cohort are available on Synapse (https://www.synapse.org/glass).

Somatic variant detection and analysis. DNA-sequencing alignment, fingerprinting, somatic variant detection (Mutect2) and copy-number segmentation were performed in accordance with the Genome Analysis Toolkit (GATK) best practices using GATK 4.0.10.1, as previously described[7,9]. Briefly, whole-exome and whole-genome reads were aligned to the b37 genome (human_g1k_v37_decoy) using BWA MEM 0.7.17. DNA fingerprint analysis using 'CrosscheckFingerprints' (Picard) confirmed that all samples belonging to a patient came from the same individual, indicating that there were no sample mismatches in this study. Somatic mutations were detected using Mutect2 (v4.1.0.0) for tumor samples with a matched normal blood sample. A panel of normals was constructed for each sequencing batch to account for differences in DNA library prep (for example, whole genome versus whole exome) and used to filter out common artifactual and germline variants. Patient tumor samples without matched normal blood were analyzed for copy-number alterations and tumor-only SNV detection was performed with a panel of normal reference according to GATK best practices. Tumor-only somatic variants were used to identify hypermutant tumors. To identify samples with increased small deletion mutation burden, the following thresholds were applied: the recurrence-specific small deletion mutation burden needed to be greater than 0.2 Mut per Mb sequenced and greater than 0.1 Mut per Mb increase when comparing all small deletion variants in the recurrence versus the primary tumor. Mutational signature estimation was performed using COSMIC v3 signatures for the GLASS and CARE datasets according to previously published methods[41]. Briefly, all WGS samples were used to generate a mutational matrix and extract de novo signatures using SigProfilerExtractor (v.1.1.4)[41] using maximum signatures set to 10 and NMF replicates set to 100. The de novo signatures were then deconvoluted to COSMIC v3.3 signatures. Finally, mutations for each sample were assigned to the most probable signature among the deconvoluted COSMIC signatures using the R package Palimpsest (v.2.0.0)[42]. Acquired SBS21 samples were denoted as those that were in the top quartile of SBS21 change at T2. For samples with matched blood, hypermutation was determined according to the cutoff of 10 Mut per Mb and further separated into de novo versus treatment-associated based on COSMIC mutational signatures. Treatment-associated hypermutation in samples with matched normal blood was classified by a longitudinal increase in mutation burden (that is, from <10 Mut per Mb to >10 Mut per Mb) and SBS11 signal (alkylating agent-associated signature). For samples without matched blood, a single recurrent sample with a large increase in mutation burden at recurrence compared to the initial tumor (18.3-fold increase) and SBS11 signature was indicative of treatment-associated hypermutation. Genetic distance between time-separated samples from the same patient was defined as the bulk DNA proportion of private mutations (SNV) and differences in CNA segments between the two samples.

Single-cell/single-nucleus data processing of human glioma samples. For droplet-based snRNA-seq data, the Cellranger v3.1.0 pipeline provided by 10x Genomics was used for alignment (GRCh38 release 93) and to generate count matrices. We quantified the gene expression levels as $E_{i,j} = \log_2(\frac{CPM_{i,j}}{10} + 1)$, where $CPM_{i,j}$ refers to counts-per-million for gene i in sample j. We divided the TPM/CPM values by 10 as the size of single-cell libraries is estimated to be in the order of 100,000 transcripts, and we, therefore, would like to avoid inflating the expression levels by counting each transcript ~10 times. Following these normalization steps, initial filtering of low-quality cells was done based on low number of detected genes (less than 200 genes) or high expression of mitochondrially encoded genes (more than 3%). The majority of low-quality cells were removed downstream in case they could not be robustly classified as malignant or nonmalignant (see in later section on CNA analysis 'Classification of cells into malignant or nonmalignant cell types'). Finally, we computed the average expression of each gene i as $\log_2((\frac{1}{n}\sum_{j=1}^{n} TPM|CPM_{i,j})+1)$

and filtered out the lowly expressed genes by limiting the analyzed genes to the top 3,000 most highly expressed genes (using the Seurat v4.0.4 (ref. [43]) function CreateSeuratObject). For the cells and genes that passed these quality control filters, we defined relative expression levels by centering the expression levels for each gene across all cells in the dataset as follows: $Er_{i,j} = E_{i,j} - \frac{1}{n}\sum_{k=1}^{n} E_{i,k}$, where n is the number of cells in the dataset.

Clustering and cell-type annotation. To facilitate clustering, cell-type annotation and scoring of droplet-based data, we used the R package Seurat (v4.0.4)[43]. Unique molecular identifier counts data were normalized and scaled (using the NormalizeData and ScaleData functions) and then clustered (by projecting the data to a lower dimensional space using principal component analysis and then running FindNeighbors and FindClusters functions). Initial classification of tumor-associated macrophages, T cells, oligodendrocytes and endothelial cells was based on the expression of known marker genes[16–19,44], whereas the rest of the cells were annotated as presumed malignant. Following classification of cells as malignant or nonmalignant (see sections 'Inferring CNAs from gene expression data' and 'Classification of cells into malignant or nonmalignant cell types'), the cells classified as nonmalignant were scored (using the AddModuleScore function) for known cell-type signatures and assigned with a cell type using the method explained in the section 'Assignment of cells to states'. Finally, heterotypic doublets were filtered out using the R package scDblFinder[45].

Inferring CNAs from gene expression data. CNAs were estimated as previously described[46–49] using the function infercna from the R package infercna (an implementation of the original method presented in ref. [50], which is available at https://github.com/jlaffy/infercna) with default parameters. Briefly, the algorithm sorts the analyzed genes in each sample according to their chromosomal location and applies a moving average with a sliding window of 100 genes within each chromosome to the relative expression values. The scores computed for the cells classified as nonmalignant (oligodendrocytes, macrophages and endothelial cells) define the baseline of normal karyotype, and their average CNA values are used to center the values of all cells.

Classification of cells into malignant or nonmalignant cell types. In cells classified using single-nucleus droplet-based sequencing, we generally encountered lower CNA signal and continuous signal distributions related to (1) lower data quality relative to that observed in single-cell data and (2) inclusion of nonmalignant cell types such as ACs and neurons in the presumed malignant group, as these cell types could not be classified a priori as nonmalignant due to transcriptional similarity with the malignant cells.

We, therefore, used a multistep classification scheme for the droplet-based single-nucleus sequencing data.

Step 1: cell classification by detection of copy-number events. For each cell j, we computed the CNA signal on each chromosome separately as $CNA_j^C = \frac{1}{n}\sum_{i=1}^{n} CNA_{i,j}^C$, where n is the number of genes on chromosome C included in the analysis. We fitted a normal distribution (that is, a classifier) to the signal distributions of the reference cells for each chromosome (using the function fitdistr from the R package MASS v.7.3-56). This enabled assigning each cell with a P value for each chromosome using a two-sided z test (function pnorm from the R package stats v.4.1.1), reflecting whether the cell has a CNA signal that is substantially different than expected from nonmalignant cells. These P values were further corrected for multiple testing (for each chromosome) using the Benjamini–Hochberg (BH) method, and cells with BH-adjusted P value < 0.05 for a particular chromosome were considered as having a copy-number event on that chromosome (either amplification or deletion based on the sign of the CNA signal). Cells with an unadjusted P value < 0.05 for a particular chromosome that failed to achieve

statistical significance following adjustment were considered to have a 'suspicious event' on that chromosome. Following this, inferred copy-number events were cross-referenced with copy-number calls from WES/WGS data, and only events detected in both methods were considered for classification and were termed 'real' events. For a subset of samples, this procedure was not possible due to (1) lack of WES/WGS data or (2) inability to call CNA events from WES/WGS due to low purity/quality. For this subset of cases, we defined a panel of highly recurring CNA events (intersection of highly recurring events inferred from snRNA-seq and WES/WGS data) that were used as a short list of potential events. Cells classified a priori as nonmalignant were reclassified as 'unresolved' in case a 'real' or 'suspicious' CNA event was detected and 'nonmalignant' otherwise. Presumed malignant cells with at least one 'real' CNA event were classified as 'malignant', those with a 'suspicious' event were classified as 'unresolved' and those with no events at all ('real' or 'suspicious') were classified as 'nonmalignant'.

Step 2: exclude questionable cells based on CNA correlation. We define the CNA correlation as the Pearson correlation between each cell and the average CNA profile of the tumor sample the cell originated from. We limit the computation to the chromosomes on which 'real' events were detected and a control panel of ~1,000 genes from other chromosomes. Based on the distribution of CNA correlations across the cells classified as Malignant, we defined 0.5 as the lower threshold of malignancy. To determine the upper threshold for nonmalignancy, we performed SNV calling from the snRNA-seq data to estimate the algorithm misclassification rate. Briefly, for each sample with available WES data, we called SNVs for each cell using the Vartrix tool (https://github.com/10XGenomics/vartrix) from the FASTQ files. Misclassified cells were defined as cells harboring a malignant mutation that were classified as nonmalignant in step 1 of the algorithm. Following a cost-effectiveness analysis (misclassification rate versus percentage of excluded cells), we set 0.35 as the upper threshold for nonmalignancy. Finally, cells classified as 'malignant' with CNAcor < 0.5 or cells classified as 'nonmalignant' with CNAcor > 0.35 were reclassified as 'Unresolved' and excluded from downstream analysis.

Step 3: refine classification by setting confidence levels. To refine the classification, we defined confidence levels. Confidence level 1 includes cells classified as malignant that harbor a malignant SNV, cells in which at least 50% of the expected CNA events were detected, including chromosome 7 amplification or chromosome 10 deletion, and cells classified as nonmalignant with CNAcor < 0.25. Confidence level 2 includes cells classified as malignant in which at least 50% of the expected CNA events were detected that do not include chromosome 7 amplification or chromosome 10 deletion, cells classified as malignant in which less than 50% of the expected CNA events were detected, including chromosome 7 amplification or chromosome 10 deletion, and cells classified as nonmalignant with CNAcor < 0.5. The rest of the cells classified as malignant or nonmalignant were assigned confidence level 3.

In the analysis presented in this work, we used only cells in confidence levels 1 and 2.

Deriving metaprograms from gene expression data. To capture the heterogeneity between cells from the same cell type, we leveraged NMF[51]. NMF was performed on the relative expression values of each sample independently after setting negative values to zero. The NMF algorithm requires defining a priori the 'k' parameter, reflecting the expected number of latent features in the data. Because 'k' varies between samples and is largely unknown, we ran the NMF algorithm on each sample using different values (3–10), thereby generating 52 programs for each sample. Each of these NMF programs was summarized by the top 50 genes based on the NMF coefficients. Derivation of the metaprograms from the NMF programs is described thoroughly in ref. 24 and will be described here briefly. The method first filters out NMF programs that are not robust (do not recur within the sample it originated from or across several samples) or are redundant within the sample (that is, it highly overlaps with other NMF programs within that sample). Following this, the robust NMF programs are clustered according to the Jaccard similarity using a customized clustering algorithm that iteratively considers the degree of overlap between robust NMF programs and combines the highly overlapping ones to form a cluster. The top 50 most recurring genes in each cluster define a metaprogram.

Overall, the algorithm yielded 16 metaprograms that were annotated based on functional enrichment analysis (using Gene Ontology (GO) terms, mSigDB Hallmark gene sets and gene sets derived from normal brain development datasets). MP 16 included genes from various cell types, resulting in a metaprogram that fits almost all cells and thereby did not reflect any heterogeneity and was therefore excluded from analysis. This same procedure was independently repeated for each nonmalignant cell type.

Assignment of cells to states. Malignant cells were scored for the NMF metaprograms using the Seurat function AddModuleScore. To facilitate cell classification, we generated 20 shuffled expression matrices by sampling 5,000 cells each time and shuffling the expression values for each gene. We then scored each shuffled matrix for the NMF metaprograms, thereby yielding 100,000 normally distributed scores for each expression program. These served as null distributions for cell state classification. For each original cell, we computed a P value for each of the expression programs with a z test (R's pnorm function) using the statistics of the null distributions that we previously generated. We adjusted all P values for multiple testing using the BH method. Each cell was classified into a specific state if the adjusted P value computed for that state was smaller than 0.05. Cells that achieved an adjusted $P < 0.05$ for multiple states were assigned to the state for which they scored maximally. Cells that did not achieve an adjusted $P < 0.05$ for any of the states were assigned an 'unresolved' state.

Cells were assigned a 'cycling' state on top of their cellular state if they achieved an adjusted $P < 0.05$ for the cell cycle metaprogram and 'noncycling' otherwise.

Hybrids detection and classification. We define hybrids as cells scoring significantly (that is, with adjusted $P < 0.05$) for at least two cellular states with a difference between the top two significant scores smaller than expected by chance. To quantify the score difference expected by chance, we leveraged the null distribution generated for the state classification algorithm and computed for each artificial cell the difference between the top two states. The 95 quantiles of this score difference distribution (equal to a difference of 0.24) were set as the threshold for determining if a state is singular or hybrid.

To estimate the expected frequency of technical hybrids, we first computed for each pair of states, (A, B), the expected frequency of hybrids, defined as $\text{Exp}(A, B) = \text{Freq}(A) \times \text{Freq}(B)$, and the O/E ratio defined as $\log_2(\frac{\text{Obs}(A,B)}{\text{Exp}(A,B)})$. As this is an overestimation of the expected frequency attributed to technical effects, we estimated this technical factor by averaging across O/E ratios of hybrid pairs detected less than expected by chance (that is, $O/E < 0$). Following this, we computed the expected frequency of technical hybrids for each hybrid pair by multiplying the expected frequency with the technical factor and defined the O/tE ratio as $\log_2(\frac{\text{Obs}(A,B)}{\text{TF} \times \text{Exp}(A,B)})$. Finally, we filtered out insignificant hybrid pairs with large O/tE ratio (attributed to small numbers) using a one-sided Fisher test. The hybrid lineage model was generated using the R package igraph with cell states as nodes and edges connecting the states that form significant hybrid pairs. We did not include the 'cycling' state in this analysis because we don't view 'cycling' as an independent state but rather as an additional feature that cells can have on top of their neurodevelopmental identity (that is, AC-like, OPC-like, etc.).

Baseline profile derivation. Each tumor sample was decomposed into seven pseudobulk profiles (one for each of the common states—AC-like, MES-like, hypoxia, GPC-like, OPC-like, NPC-like and NEU-like—given at least 25 cells classified to the particular state) by averaging across the normalized unique molecular identifier counts and $\log_2$-transforming. Genes were included if their mean $\log_2$-expression value across all pseudobulks was at least 1 and if their median variance (computed separately within state) was at least 2.5. Overall, 1,005 genes passed these filters. Following this, the pseudobulks were analyzed within the state to remove the state-specific signal using principal component analysis. We then derived six gene programs from each state (top and bottom 50 genes of the first three principal components), computed the Jaccard similarity index between each pair of programs and clustered the similarity matrix using hierarchical clustering. This revealed five distinct clusters from which we derived five consensus signatures by including genes that recurred in at least 25% of programs in each of the clusters (with a hard minimum of at least three times). By manual inspection and GO enrichment, we annotated the consensus signatures. Two signatures were excluded due to short length or high suspicion of reflecting a technical artifact. To exclude the possibility that ambient RNA has a role in driving the baseline profiles, we estimated per sample using the R package SoupX the contamination by ambient RNA. There was no difference in the estimated contamination level across the different baseline profiles as well as no significant overlap between the topmost contaminated genes per sample and the metaprogram or baseline profile signatures (data not shown due to lack of significance).

Assigning tumors to composition groups. To measure the differences in tumor composition, we generated for each tumor sample a composition vector reflecting the proportion of each cell type in the tumor sample. This enabled assigning tumors to the following three main composition groups: HMF (percentage of malignant cells >75%), IMF (percentage of malignant cells, 50–75%) and LMF (malignant cells <50%), where the LMF group could be further subdivided according to the dominant TME cell types (percentage of TAM/oligodendrocyte/glio-neural >40%, or mixed in case of no dominant TME cell type). Similarly, we defined proportion vectors for the malignant cell states and assigned tumors to six groups according to the dominant cell state (at least 25% of cells assigned to the particular state)—AC, MES/hypoxia, GPC, OPC/NPC, neuron and mixed (in case of no dominant state). Tumors were classified according to the baseline profile with a maximal score and to the mixed category if the maximal score was less than 0.25.

Multilayer group definition. The association between each pair of features (A, B) was computed using a binomial test with the number of times the pair was observed as the number of successes, the number of tumor samples as the number of experiments and the frequency of feature A times the frequency of feature B as the expected probability of success (under the assumption that the features are independent). We then generated an undirected graph by defining each feature as a node and connecting the nodes with edges in case a statistically significant association (unadjusted for multiple testing) between the two features was observed.

Measuring transcriptional distance between matched pairs. To measure the transcriptional distance between matched pairs, we generated state-controlled pseudobulk profiles from each pair. State control was achieved by downsampling both samples to 25 cells from each state, given that both samples contain at least 25 cells from the particular state, resulting in samples that contain the same number of cells and are balanced across the different gene expression profiles of the cellular states. Following this, the pseudobulk profiles were computed by averaging for each gene across the selected cells, resulting in two pseudobulk profiles. Finally, the Euclidean distance

between the two vectors was computed and served as the metric for transcriptional distance.

Survival analysis. Survival analysis was performed using the R packages survival v.3.3-1 and survminer v.0.4.9. Kaplan–Meier estimates were computed using the survfit function and plotted using the ggsurvplot function (survminer package). Statistical significance of the difference between the survival curves was computed using the log-rank test (implemented in the function survdiff). Cox regression analysis and forest plots were performed and plotted using the same packages (coxph and ggforest functions).

Differentially expressed genes between *MGMT*-low and *MGMT*-high pairs. To compute the differentially expressed genes between *MGMT*-low and *MGMT*-high pairs, we first computed the relative gene expression across time points in each group (that is, longitudinal expression difference), which is defined for each gene i as the average expression of the gene across all T2 samples in the group minus the average gene expression across all T1 samples in the group. Following, we computed the Euclidean distance between these two vectors. *MGMT*-low genes were defined as the top 100 genes with the largest distance between the groups and positive longitudinal expression difference in the *MGMT-low* group and negative longitudinal expression difference in the *MGMT*-high group. *MGMT*-high genes were defined as the top 100 genes with the largest distance between the groups and positive longitudinal expression difference in the *MGMT*-high group and negative longitudinal expression difference in the *MGMT*-low group.

Reporting summary

Further information on research design is available in the Nature Portfolio Reporting Summary linked to this article.

Data availability

Processed snRNA-seq data generated for this study are available at the Gene Expression Omnibus under accession GSE274546 (10x Genomics). All de-identified somatic mutation calls, copy-number alteration calls and genomic analysis tables are available via Synapse (https://www.synapse.org/care_glioblastoma). Raw sequencing data are available with limitations in accordance with consent forms from the Data Use Oversight System (DUOS) at https://duos.broadinstitute.org/ under the following IDs: DUOS-000475, DUOS-000476, DUOS-000477, DUOS-000478, DUOS-000479 and DUOS-000480.

Code availability

Analysis scripts used in this study are available at GitHub (https://github.com/dravishays/GBM-CARE-WT) and Zenodo[52] (https://doi.org/10.5281/zenodo.14966015). Scripts for processing DNA-sequencing data can be accessed at https://github.com/Kcjohnson/care-glass.

References

41. Islam, S. M. et al. Uncovering novel mutational signatures by de novo extraction with SigProfilerExtractor. *Cell Genom.* **2**, 100179 (2022).

42. Shinde, J. et al. Palimpsest: an R package for studying mutational and structural variant signatures along clonal evolution in cancer. *Bioinformatics* **34**, 3380–3381 (2018).

43. Hao, Y. et al. Integrated analysis of multimodal single-cell data. *Cell* **184**, 3573–3587.e29 (2021).

44. Velmeshev, D. et al. Single-cell genomics identifies cell type-specific molecular changes in autism. *Science* **364**, 685–689 (2019).

45. Germain, P., Lun, A., Meixide, C. G., Macnair, W. & Robinson, M. D. Doublet identification in single-cell sequencing data using scDblFinder. *F1000Res.* **10**, 979 (2021).

46. Neftel, C. et al. An integrative model of cellular states, plasticity, and genetics for glioblastoma. *Cell* **178**, 835–849.e21 (2019).

47. Tirosh, I. et al. Single-cell RNA-seq supports a developmental hierarchy in human oligodendroglioma. *Nature* **539**, 309–313 (2016).

48. Venteicher, A. S. et al. Decoupling genetics, lineages, and microenvironment in IDH-mutant gliomas by single-cell RNA-seq. *Science* **355**, eaai8478 (2017).

49. Tirosh, I. et al. Dissecting the multicellular ecosystem of metastatic melanoma by single-cell RNA-seq. *Science* **352**, 189–196 (2016).

50. Patel, A. P. et al. Single-cell RNA-seq highlights intratumoral heterogeneity in primary glioblastoma. *Science* **344**, 1396–1401 (2014).

51. Gaujoux, R. & Seoighe, C. A flexible R package for nonnegative matrix factorization. *BMC Bioinformatics* **11**, 367 (2010).

52. Spitzer, A., Johnson, K., Nomura, M. & Garofano, L. The multi-layered transcriptional architecture of glioblastoma ecosystems. *Zenodo* https://doi.org/10.5281/zenodo.14966015 (2025).

Author contributions

A.S., K.C.J., M.N., L.G., A. Lasorella, A.I., R.G.W.V., I.T. and M.L.S. conceived and designed the project. M.N., F.S.V., K.J.A. and Y.T.O. led the data generation. A.S., K.C.J., L.G. and I.T. performed computational analyses. D.N., N.G.D., A.C.G., L.B., F.S.V., F.D., S.G., K.J.A., S.M., F.D., L.N.G.C., T.C., N.R., C.R. and J.B.P. provided experimental and analytical support. A. Lipsa, F.H., A.G., S.P.N., L.N., S.K., S.D., H.E.M., S.H.P., F.B., A. Laurenge, A.L.D.S., B.M., A.P., M.S., S.T., N.S., D.M.A., S.T.K., J.T.H., W.K.A.Y. and K.L.L. provided patient samples and curated the clinical annotation. A.S., K.C.J., M.N., L.G., A. Lasorella, A.I., R.G.W.V., I.T. and M.L.S. wrote the paper, with feedback from all authors. A.I., A. Lasorella, R.G.W.V., I.T. and M.L.S. jointly supervised this work and interpreted the results.

Competing interests

M.L.S. is an equity holder, scientific cofounder and advisory board member of Immunitas Therapeutics. I.T. is an advisory board member of Immunitas Therapeutics and a scientific cofounder of Cellyrix. R.G.W.V. is a cofounder and equity holder in Boundless Bio. The authors declare that such activities have no relationship to the present study. The other authors declare no competing interests.

Additional information

Extended data is available for this paper at https://doi.org/10.1038/s41588-025-02168-4.

Supplementary information The online version contains supplementary material available at https://doi.org/10.1038/s41588-025-02168-4.

Correspondence and requests for materials should be addressed to Anna Lasorella, Antonio Iavarone, Roel G. W. Verhaak, Itay Tirosh or Mario L. Suvà.

Peer review information *Nature Genetics* thanks Richard Gilbertson, Wolfgang Wick and the other, anonymous, reviewer(s) for their contribution to the peer review of this work.

Reprints and permissions information is available at www.nature.com/reprints.

a

b

c
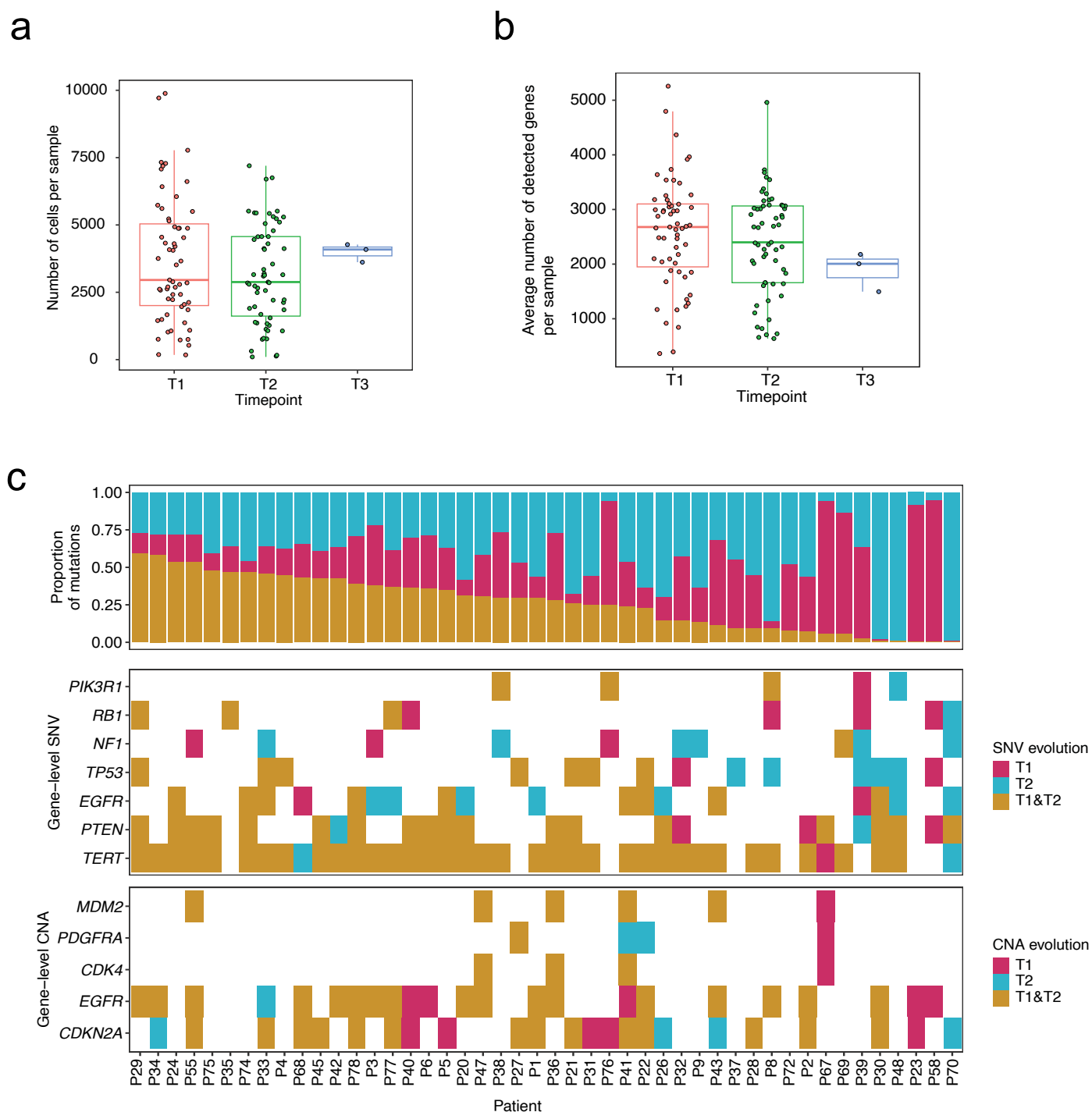
Extended Data Fig. 1 | Longitudinal profiling of a clinically annotated GBM cohort. a, Number of cells per sample (post QC) across the 3 time points. Each point represents a sample. There are no statistically significant differences between the groups (tested with two-sided Kruskal–Wallis test, *p* = 0.51). **b**, Average number of detected genes per sample (post QC) across the 3 time points. Each point represents a sample. There are no statistically significant differences between the groups (tested with two-sided Kruskal–Wallis test,

p = 0.27). **c**, Overview of SNV and CNA in the GBM cohort. Each column represents a single patient with longitudinal DNA data and a matched normal blood sample. The top panel indicates the total proportion of mutations that are either detected across both T1 and T2 (that is, shared), only in T1 or only in T2, which are sorted by decreasing shared mutation fraction. The middle panel represents the mutation variant status for driver genes in GBM, while the bottom panel presents the driver CNAs.
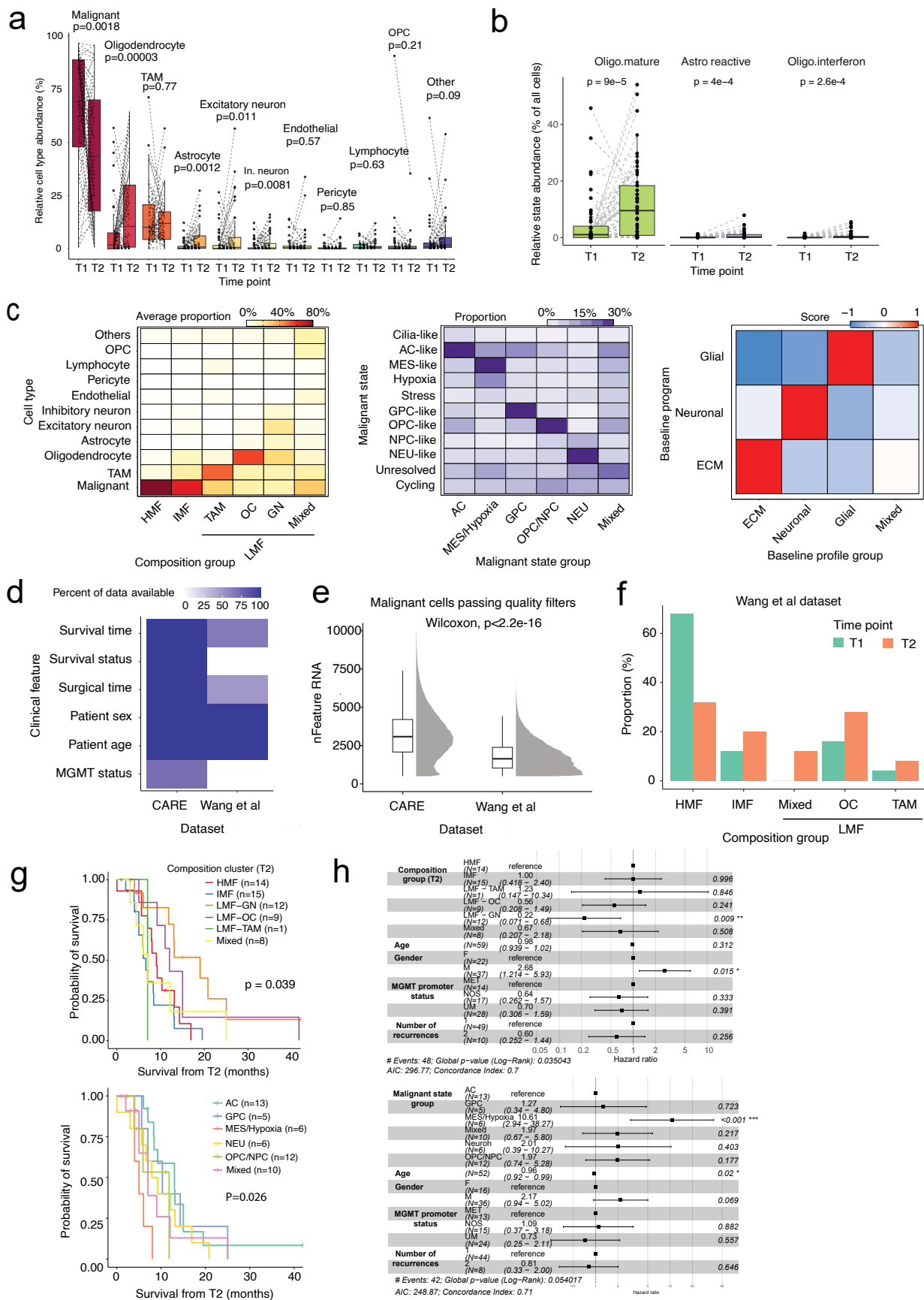
Extended Data Fig. 2 | See next page for caption.

Extended Data Fig. 2 | Longitudinal cell-type changes in the TME, global similarity of cell states between primary and recurrent samples and prognostically significant cell-type profiles. a, Relative granular cell-type abundance across the two time points (primary and recurrence). Unadjusted two-sided paired Wilcoxon rank-sum test is shown (n = 56 patients). Dotted lines connect patient values. **b**, Relative granular non-malignant cell state abundance across the two time points (primary and recurrence) that showed statistical significance between time points following adjustment for multiple comparisons. Unadjusted two-sided paired Wilcoxon rank-sum test is shown (n = 56 patients). Dotted lines connect patient values. **c**, Average proportion of cellular composition (left) of malignant cell state composition (middle) and average baseline profile score (right) for each feature group. **d**, Available clinical data information for this study and ref. 14 dataset. **e**, Comparison of the number of detected genes per cell in cells passing quality filters between this study and ref. 14 dataset. Two-sided Wilcoxon rank-sum test is shown. Box plots span from the first to third quartiles, median values are indicated by a horizontal line, whiskers show 1.5× interquartile range and outlier points are not shown. Continuous distributions of all values are shown to the right of each box plot. **f**, Proportion (%) of samples from ref. 14 assigned to each compositional group across the two time points (primary and recurrence). **g**, Kaplan–Meier curves depicting the survival time after 2nd resection according to the transcriptomic features at 2nd resection, which shows the statistical significance in the distribution between groups. Top panel is for composition group. Bottom panel is for malignant state groups. Statistical significance of survival difference between the groups in each panel was computed using the log-rank test. **h**, Forest plot reflects Cox proportional hazard model for time from 2nd resection to outcome, including relevant biological and clinical covariates in addition to composition group (top) and malignant state group (bottom). Each variable is presented along with its categorical possibilities and sample size on the left, while the boxes represent the hazard ratio and lines represent the 95 % confidence interval.
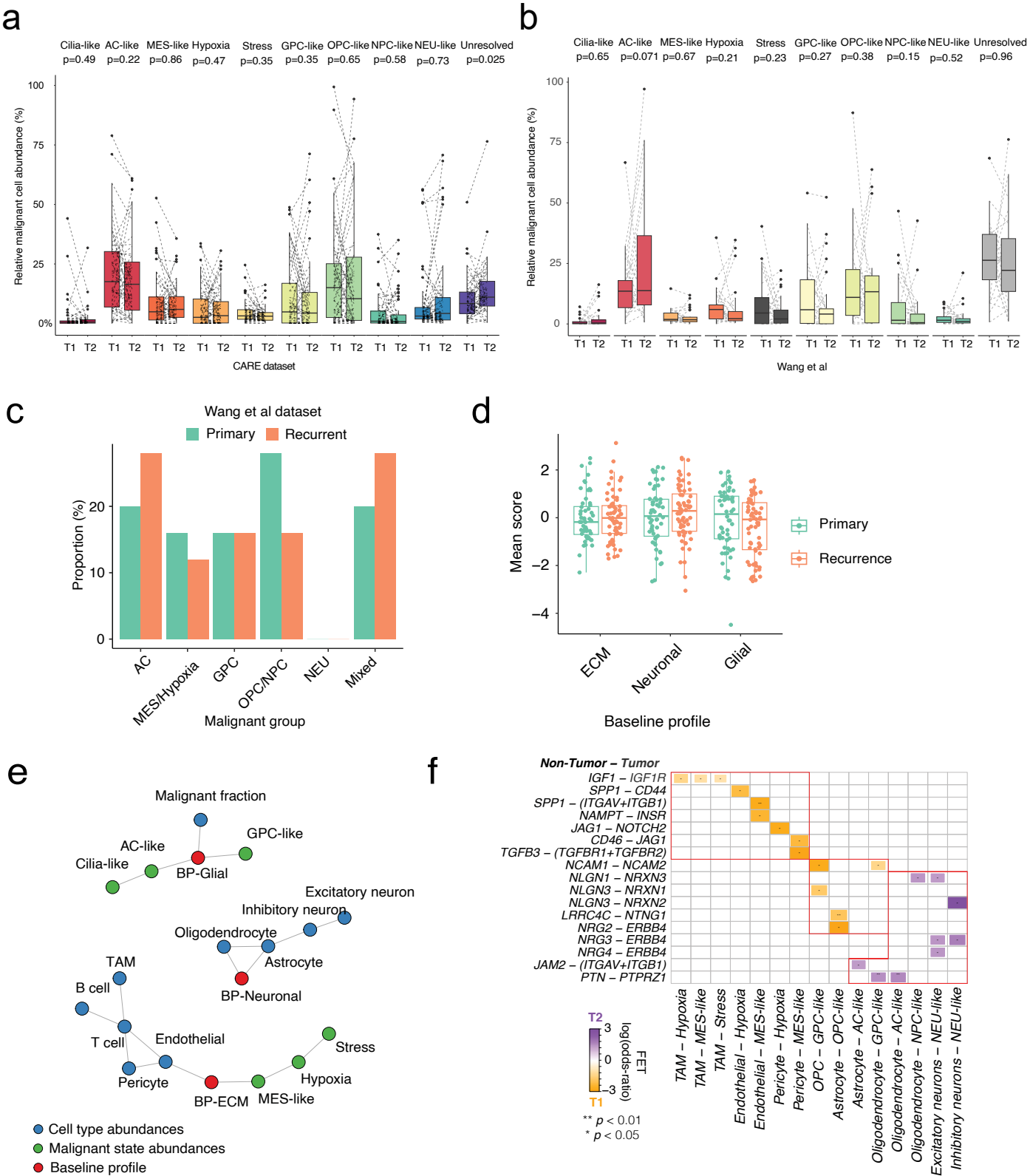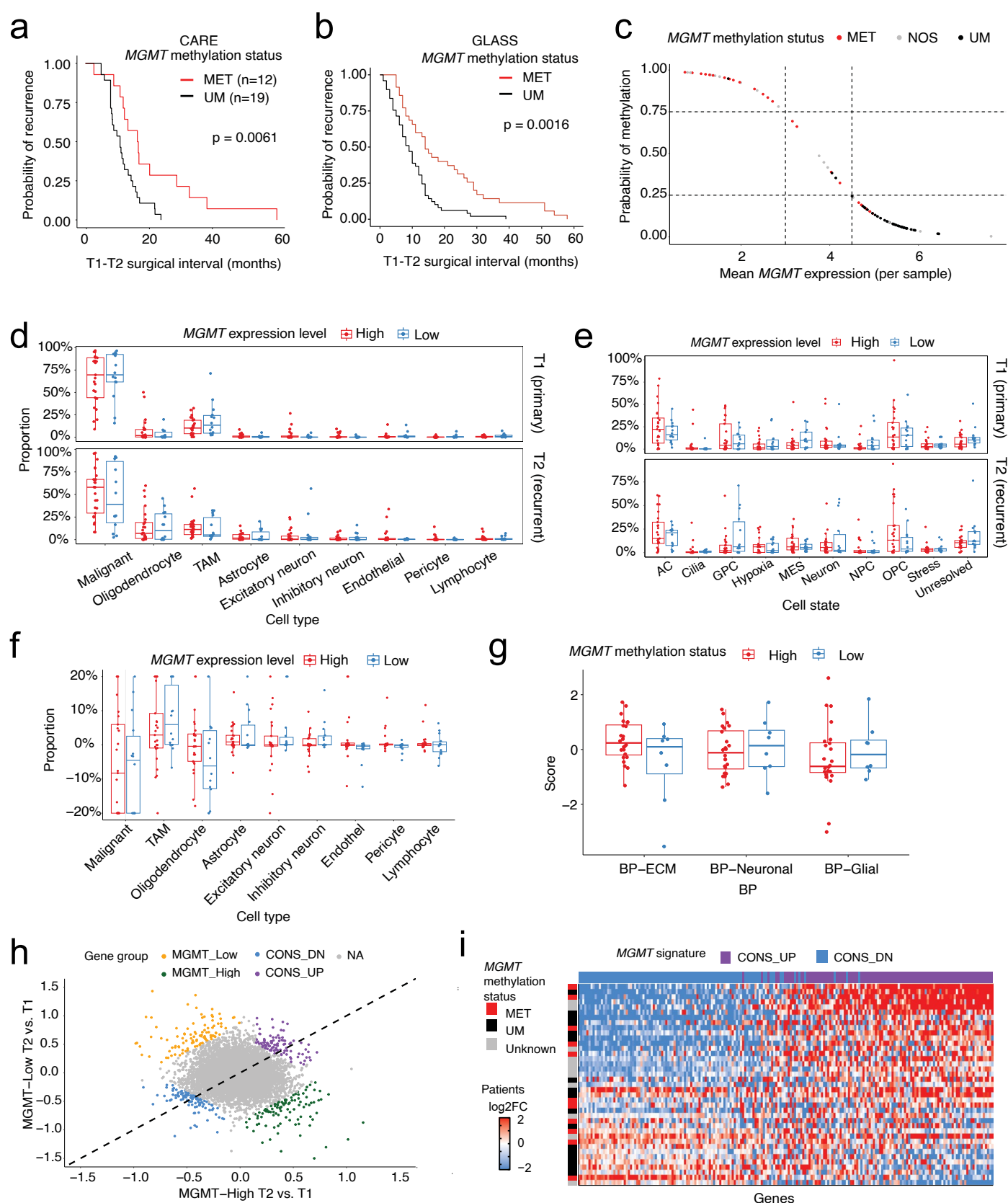
Extended Data Fig. 3 | See next page for caption.

Extended Data Fig. 3 | Malignant state abundance and malignant-TME interactions across time points. a,b, Malignant cell state abundance across time points. Dotted lines connect patient values. Unadjusted two-sided paired Wilcoxon rank-sum tests are shown. **a**, This study (n = 50 patients with at least 50 malignant cells in both time points). **b**, ref. 14 dataset. (n = 25 patients). **c**, Proportion (%) of tumors in each malignant group in the ref. 14 dataset. **d**, Box plots of the average BP scores per sample across the two time points. **e**, Interaction graph of associations between features conserved across time points. Edges represent statistically significant (p < 0.05) Pearson correlation in both time points. **f**, Heatmap of ligand–receptor cross-talks. Each row represents a ligand–receptor interaction, while each column represents a non-malignant cell type–malignant cell state pair, such that the ligand is expressed by the corresponding non-malignant cell type and the receptor by the malignant cell state. The colors represent the log(odds ratio) from the two-sided Fisher's exact test for checking whether the ligand–receptor interaction is significantly present in T2 (log(odds ratio >0), purple scale) or T1 (log(odds ratio <0), orange scale). Only significant interactions are reported in the heatmap (**p < 0.01, *p < 0.05).

a

b
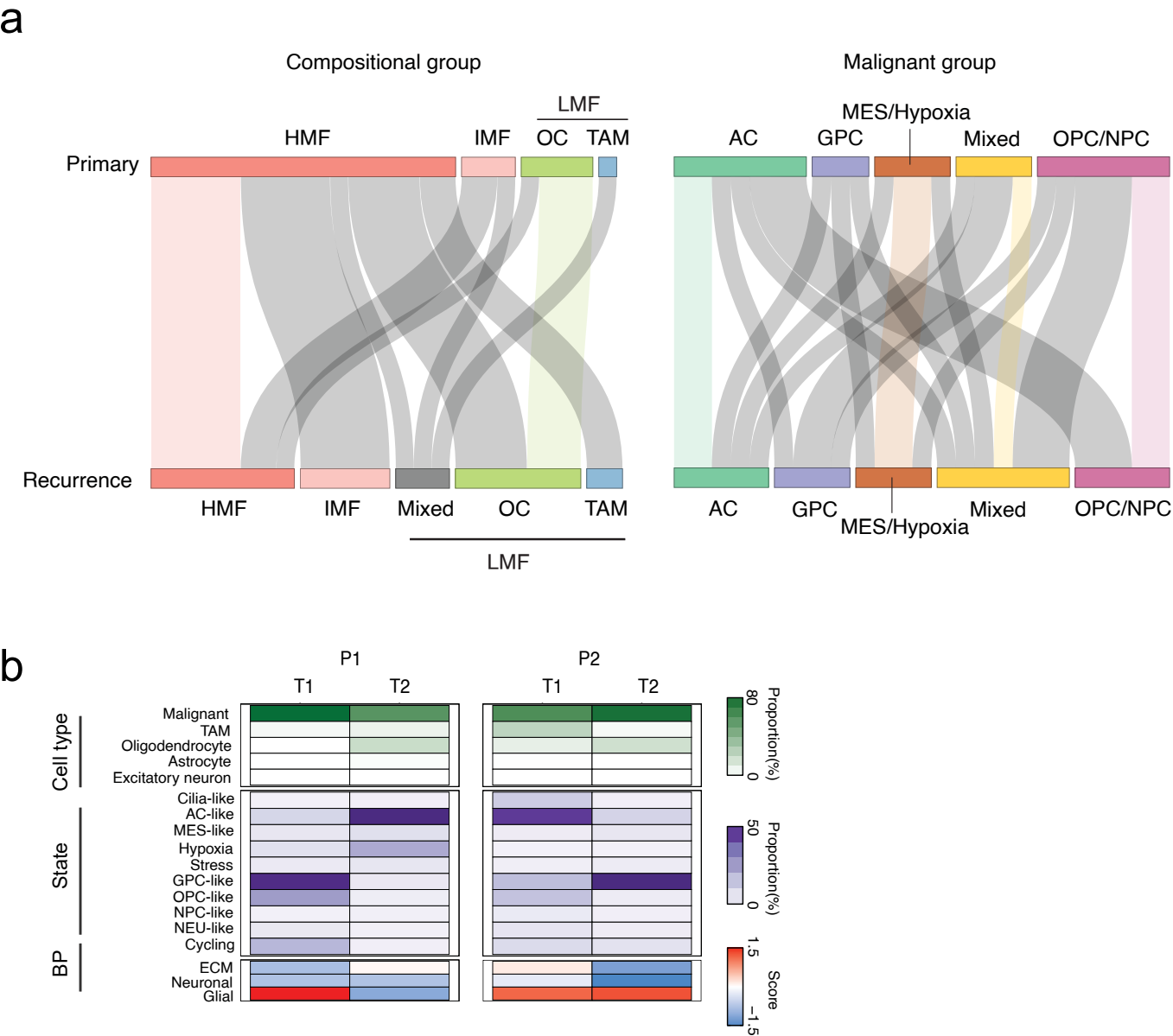
Extended Data Fig. 4 | Divergence of individual sample pairs. a, Sankey plots depicting the transitions between time points across malignant states for ref. 14 dataset. **b,** Representative two pairs that showed opposite longitudinal transcriptomic changes in the two pairs profiled at two time points highlight unpredictable gene expression trajectories. Heatmap representing three transcriptomic layers between time points are shown.

Extended Data Fig. 5 | See next page for caption.

Extended Data Fig. 5 | MGMT expression in GBM single cells influences recurrence trajectories. a, Surgical interval for the patients included in this analysis stratified by the *MGMT* promoter methylation status. X axis reflects the time from 1st to 2nd resection. Statistical significance of survival difference between the groups in each panel was computed using the log-rank test. **b**, Surgical interval analysis for the IDH-wildtype patients in the GLASS cohort stratified by the *MGMT* promoter methylation status. X axis reflects the time from 1st to 2nd resection. Statistical significance of survival difference between the groups in each panel was computed using the log-rank test. **c**, Logistic regression model using the average of *MGMT* gene expression in primary samples to infer the *MGMT* methylation status in the ref. 14 dataset. **d**, Proportion (%) of each cell type across the two time points (primary and recurrence) stratified by *MGMT* expression level. For **d**–**g**, box plots represent the median value as a solid horizontal line, lower and upper edges correspond to the first and third quartiles

(the 25th and 75th percentiles), and the whiskers represent plus and minus 1.5× the interquartile range. Individual sample values are shown as jittered points. **e**, Proportion (%) of each malignant cell state across the two time points (primary and recurrence) stratified by *MGMT* expression level. **f**, Difference within patients in proportion (% in R − % in P) of each cell type across *MGMT* expression levels. **g**, Difference within patients in BP scores (score in R − score in P) across *MGMT* expression levels. **h**, Differentially expressed genes between *MGMT*-low and high groups across the recurrence trajectories (Methods). Each dot represents a gene, and dots are colored according to the group of DE genes to which they belong. **i**, CONS-UP and CONS-DN signatures plotted for patients included in the analysis. Value represents the T2–T1 difference ($\log_2$(FC) of gene expression) for each patient. Patients are ordered according to the difference between signature scores. Genes are ordered according to their correlation (across patients) with the difference between signature scores.
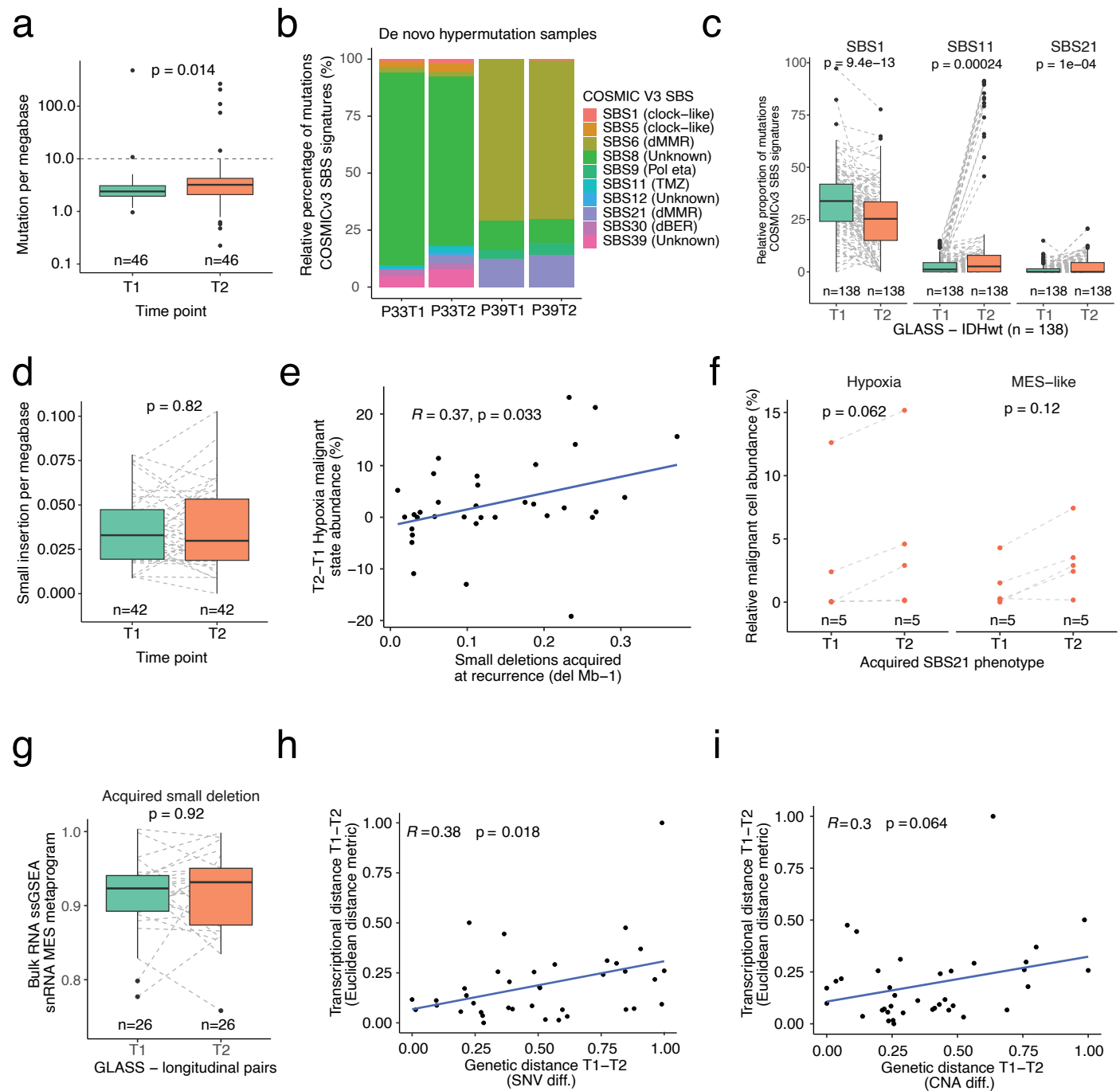
Extended Data Fig. 6 | Mutational signatures associated with recurrence trajectories. a, Mutation burden at both time points for patients with matched normal blood DNA (n = 46 samples per time point, two-sided paired Wilcoxon test). **b**, COSMIC v3 mutational signature contribution for two patients with high mutation burden at both time points with minimal contribution from SBS11 (alkylating agent signature). **c**, Selected single base substitution (SBS) mutational signature proportions for GLASS IDH-wildtype cases for both time point 1 and time point 2. Dotted lines connect samples from the same patients. SBS1 (aging/clock-like etiology), SBS11 (alkylating agent) and SBS21 (defective mismatch repair). P values represent two-sided paired Wilcoxon rank-sum test. **d**, Longitudinal difference in small insertion burden between T1 and T2 with dotted lines connecting patient values. Analysis restricted to non-hypermutant cases. P-value reflects two-sided paired Wilcoxon rank-sum test. **e**, Longitudinal change (T2–T1) in the hypoxia cell state abundance is plotted on the y axis

against the small deletion burden specific to the recurrent tumor with the linear regression line shown in blue. The Pearson correlation coefficient and *P* value are presented. **f**, Longitudinal change in the hypoxia and MES-like cell state relative abundances for patients that acquired SBS21 mutations but that did not acquire small deletion burden increase. **g**, Bulk RNA data from the GLASS consortium were scored for the MES-like snRNA malignant metaprogram signature, and the relative single-sample gene set enrichment analysis (ssGSEA) score is presented on the y axis. The panel shows the longitudinal change in the MES-like signature for those patients whose tumor had a small deletion increase. P value from paired Wilcoxon rank-sum test. **h,i**, Scatterplots that represent the scaled genetic distance for SNVs (proportions of private mutations) **h**, and CNAs (differences in copy-number altered regions, **i**, versus scaled transcriptional distance (snRNA). Shown is the Pearson's correlation coefficient, associated P value, with the linear regression line shown in blue for both **h** and **i**.

nature portfolio

Corresponding author(s): Mario L. Suvà, Itay Tirosh, Roel G.W. Verhaak, Antonio Iavarone, Anna Lasorella

Last updated by author(s): Mar 7, 2025

Reporting Summary

Nature Portfolio wishes to improve the reproducibility of the work that we publish. This form provides structure for consistency and transparency in reporting. For further information on Nature Portfolio policies, see our Editorial Policies and the Editorial Policy Checklist.

Statistics

For all statistical analyses, confirm that the following items are present in the figure legend, table legend, main text, or Methods section.

n/a	Confirmed	
☐	☒	The exact sample size (*n*) for each experimental group/condition, given as a discrete number and unit of measurement
☐	☒	A statement on whether measurements were taken from distinct samples or whether the same sample was measured repeatedly
☐	☒	The statistical test(s) used AND whether they are one- or two-sided *Only common tests should be described solely by name; describe more complex techniques in the Methods section.*
☐	☒	A description of all covariates tested
☐	☒	A description of any assumptions or corrections, such as tests of normality and adjustment for multiple comparisons
☐	☒	A full description of the statistical parameters including central tendency (e.g. means) or other basic estimates (e.g. regression coefficient) AND variation (e.g. standard deviation) or associated estimates of uncertainty (e.g. confidence intervals)
☐	☒	For null hypothesis testing, the test statistic (e.g. *F*, *t*, *r*) with confidence intervals, effect sizes, degrees of freedom and *P* value noted *Give P values as exact values whenever suitable.*
☒	☐	For Bayesian analysis, information on the choice of priors and Markov chain Monte Carlo settings
☒	☐	For hierarchical and complex designs, identification of the appropriate level for tests and full reporting of outcomes
☐	☒	Estimates of effect sizes (e.g. Cohen's *d*, Pearson's *r*), indicating how they were calculated

Our web collection on statistics for biologists contains articles on many of the points above.

Software and code

Policy information about availability of computer code

Data collection	No software was used for data collection.
Data analysis	Data analysis was performed in R v4.1.1. Cellranger v3.1.0 pipeline was used to generate count matrices from Illumina base calls. Packages used and versions follow below. survminer_0.4.9, survival_3.3-1, viridis_0.6.2, viridisLite_0.4.0, RColorBrewer_1.1-3, NMF_0.24.0, synchronicity_1.3.5, bigmemory_4.5.36, Biobase_2.52.0, BiocGenerics_0.38.0, cluster_2.1.3, rngtools_1.5.2, pkgmaker_0.32.2, registry_0.5-1, igraph_1.3.0, BiocParallel_1.26.2, purrr_1.0.1, Matrix_1.3-4, circlize_0.4.13, ComplexHeatmap_2.8.0, scalop_1.1.0, infercna_1.0.0, ggridges_0.5.3, ggpubr_0.4.0, reshape2_1.4.4, scales_1.2.1, ggplot2_3.4.1, patchwork_1.1.1, SeuratObject_4.0.2, Seurat_4.0.4, tibble_3.1.6, dplyr_1.1.0, MASS_7.3-56, GATK (including Mutect2) v4.1.0.0, enrichplot_1.12.2, psych_2.2.3, ggrastr_1.0.1, scDblFinder_1.6.0, SoupX_1.6.2

For manuscripts utilizing custom algorithms or software that are central to the research but not yet described in published literature, software must be made available to editors and reviewers. We strongly encourage code deposition in a community repository (e.g. GitHub). See the Nature Portfolio guidelines for submitting code & software for further information.

Data

Processed snRNA-seq data generated for this study are available through the Gene Expression Omnibus (GEO) under the following accession codes: GSE274546 and GSE274548. Raw snRNA-seq data is available with limitations in accordance with consent forms from the Data Use Oversight System (DUOS) at https://duos.boardinstitute.org under IDs: DUOS-000475; DUOS-000476; DUOS-000477; DUOS-000478; DUOS-000479; and DUOS-000480. Processed bulk DNA sequencing data (whole exome sequencing (WXS) and whole genome sequencing (WGS)) from these samples are available at https://www.synapse.org/care_glioblastoma. Previously published bulk RNA-seq data and bulk WES/WGS data from the GLASS cohort reanalyzed in this study are available at https://www.synapse.org/glass. Previously published single cell RNA-seq data reanalyzed in this study are available under GSE131928 (Neftel 2019). Previously published single cell RNA-seq data reanalyzed in this study are available under EGAS00001004909 (Wang 2019).

Research involving human participants, their data, or biological material

Policy information about studies with human participants or human data. See also policy information about sex, gender (identity/presentation), and sexual orientation and race, ethnicity and racism.

Reporting on sex and gender	The study analyzed adult glioblastoma samples. Patients were male and female. The covariate-relevant population characteristics of the human research participants are provided in Supplementary Table 1.
Reporting on race, ethnicity, or other socially relevant groupings	Primary and matched recurrent glioblastoma samples longitudinally collected in 7 hospitals were analyzed in this study.
Population characteristics	Human glioblastoma samples were provided by 7 hospitals in 6 countries (USA, Canada, France, Luxembourg Japan, and Republic of Korea). The covariate-relevant population characteristics of the human research participants are provided in Supplementary Table 1.
Recruitment	Primary and matched recurrent glioblastoma samples longitudinally collected in 7 hospitals were used in this study.
Ethics oversight	Collection was approved by the Institutional Review Board of following institutions, and all patients provided informed consent accordingly: The Institutional Review Board of MD Anderson Cancer Center (protocol number 2012-0441), The Institutional Review Board of Duke University Hospital (protocol number Pro0007434), the Institutional Review Board of Tokyo University Hospital (protocol number G10028), the Institutional Review Board of Pitie-Salpetriere Hospital (certification# 96-900), the Institutional Review Board of St. Michael's Hospital (protocol number REB # 13-14), the Institutional Review Board of Seoul National University Hospital (approval number H-2004-049-1116), the Institutional Review Board of Centre Hospitalier de Luxembourg (protocol number 201201/06).

Note that full information on the approval of the study protocol must also be provided in the manuscript.

Field-specific reporting

Please select the one below that is the best fit for your research. If you are not sure, read the appropriate sections before making your selection.

☒ Life sciences   ☐ Behavioural & social sciences   ☐ Ecological, evolutionary & environmental sciences

For a reference copy of the document with all sections, see nature.com/documents/nr-reporting-summary-flat.pdf

Life sciences study design

All studies must disclose on these points even when the disclosure is negative.

Sample size	Sample size was determined by the availability of donor and patient-derived material. We performed single-nucleus RNAseq for 121 glioblastoma samples derived from 59 patients.
Data exclusions	No data were excluded from the study.
Replication	This study doesn't include in vivo or in vitro experiments. Findings were validated by analysis of publicly available single-nucleus RNAeq data.
Randomization	Randomization is not applicable as no experimental groups were used in this study.
Blinding	Blinding was not applicable to this study since no effect for treatment or perturbations to the system were assesed.

Reporting for specific materials, systems and methods

We require information from authors about some types of materials, experimental systems and methods used in many studies. Here, indicate whether each material, system or method listed is relevant to your study. If you are not sure if a list item applies to your research, read the appropriate section before selecting a response.

Materials & experimental systems

n/a	Involved in the study
☒	Antibodies
☒	Eukaryotic cell lines
☒	Palaeontology and archaeology
☒	Animals and other organisms
☒	Clinical data
☒	Dual use research of concern
☒	Plants

Methods

n/a	Involved in the study
☒	ChIP-seq
☒	Flow cytometry
☒	MRI-based neuroimaging

Plants

Seed stocks	*Report on the source of all seed stocks or other plant material used. If applicable, state the seed stock centre and catalogue number. If plant specimens were collected from the field, describe the collection location, date and sampling procedures.*
Novel plant genotypes	*Describe the methods by which all novel plant genotypes were produced. This includes those generated by transgenic approaches, gene editing, chemical/radiation-based mutagenesis and hybridization. For transgenic lines, describe the transformation method, the number of independent lines analyzed and the generation upon which experiments were performed. For gene-edited lines, describe the editor used, the endogenous sequence targeted for editing, the targeting guide RNA sequence (if applicable) and how the editor was applied.*
Authentication	*Describe any authentication procedures for each seed stock used or novel genotype generated. Describe any experiments used to assess the effect of a mutation and, where applicable, how potential secondary effects (e.g. second site T-DNA insertions, mosiacism, off-target gene editing) were examined.*